UNIVERSIDAD DE CONCEPCIÓN

Centro de Investigación en Ingeniería Matemática (CI^{2}MA)

Coupled finite volume methods for settling in inclined vessels with natural convection

Fernando Betancourt, Raimund Bürger,
Julio Careaga, Lucas Romero

PREPRINT 2024-09

SERIE DE PRE-PUBLICACIONES

COUPLED FINITE VOLUME METHODS FOR SETTLING IN INCLINED VESSELS WITH NATURAL CONVECTION

FERNANDO BETANCOURT[A], RAIMUND BÜRGER[B], JULIO CAREAGA[C,*], AND LUCAS ROMERO[B]

Abstract. A widely applied technology of gravity-driven solid-liquid separation in mineral processing is the use of lamella settlers. These units are continuously operated tanks equipped with a number of parallel inclined plates immersed in the mixture to be separated. The inclination of the plates exploits the well-known Boycott effect that describes the enhancement of settling rates beneath inclined surfaces. This effect is usually attributed to a rapidly upward-streaming layer of clear liquid. The essence of this effect can be studied by examining gravity settling in an inclined tube or rectangular channel. The lower and upper surfaces of the channel represent the plate onto which the particles start to settle and below which the clarified liquid streams upward, respectively. In addition an increase of temperature in some part of the fluid causes a local change in the density of the fluid and circulation of the fluid within the vessel. It has been proposed to exploit this behaviour to accelerate the settling process by additional heating. To examine this hypothesis a model and corresponding numerical method to describe inclined settling enhanced by natural convection are formulated. The model consists in a two-dimensional scalar conservation law for the solids concentration coupled with a version of the Stokes system that accounts for density fluctuations in the mixture enhanced by a Boussinesq approximation of the effect of temperature. In addition a convection-diffusion equation describes heat transport and diffusion. The main outcome is a numerical method that allows one to simulate the effect of controllable parameters such as the initial concentration, difference of temperature, and angle of inclination on the progress of the solid-liquid separation. Numerical examples are presented. Results reconfirm that the enhancement of settling rates depends critically on the dimensions of the settling vessel, intensity of heating, and particle size, and is marginal for settling of relatively large particles and channels with a moderate length to width aspect ratio.

1 Introduction

1.1 Scope

Solid-liquid separation processes in mineral processing are usually driven by gravity (sedimentation), centrifugal force (centrifugation), or an applied pressure (filtration). Widely applied current technologies include lamella settlers (that are also known as lamella clarifiers, inclined plate settlers, or lamella separators). These units are continuously operated tanks equipped with a number of parallel inclined plates immersed in the mixture to be separated (see Figure 1). Settling in such

Date: May 14, 2024.

Key words and phrases. Sedimentation, natural convection, Boycott effect, numerical simulation, lamella settler.

*Corresponding author.

[A]CI^{2}MA and Departamento de Ingeniería Metalúrgica, Facultad de Ingeniería, Universidad de Concepción, Casilla 160-C, Concepción, Chile. E-Mail: fbetancourt@udec.cl.

[B]CI^{2}MA and Departamento de Ingeniería Matemática, Facultad de Ciencias Físicas y Matemáticas, Universidad de Concepción, Casilla 160-C, Concepción, Chile. E-Mail: rburger@ing-mat.udec.cl, lucasromero@udec.cl

[C]Departamento de Matemática, Universidad del Bío-Bío, Concepción, Chile. E-Mail: jcareaga@ubiobio.cl

.

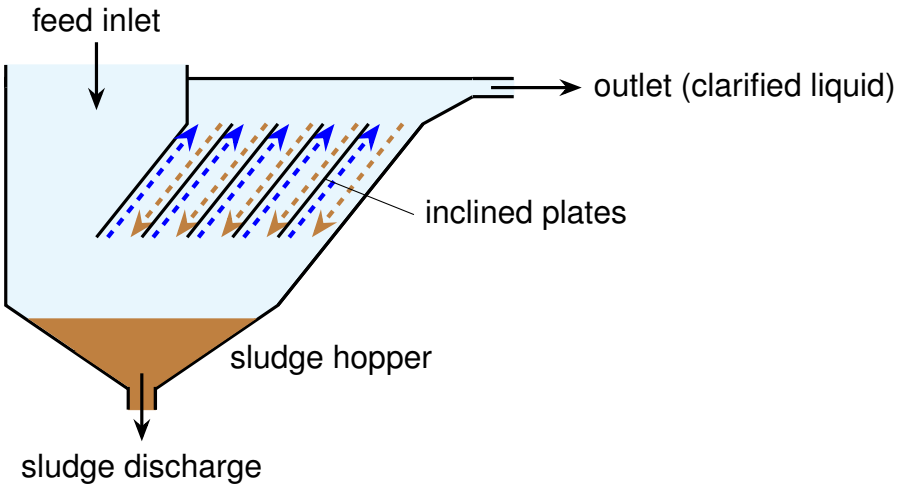

FIGURE 1. Schematic of a lamella settler.

an equipment takes place solely due to gravity forces. The inclination of the plates is therefore chosen such that purely vertical sedimentation is avoided and the well-known Boycott effect [4] is exploited. The latter effect describes the increase of settling rates beneath inclined surfaces.

The flow and solid-liquid separation between inclined parallel plates can be studied by examining gravity settling in a tube or rectangular channel with an angle of inclination identical to that of the lamella settler. The lower and upper surfaces of the channel represent the plate onto which the particles start to settle and below which the clarified liquid streams upward, respectively. We herein focus on describing on the effect of influencing the process by natural convection. In fact, an increase of temperature in some part of the fluid causes a local change in the density of the fluid, which as consequence causes circulation of the fluid within the vessel. It has been proposed [35] to exploit this behaviour to accelerate the settling process.

It is the purpose of this contribution to present a mathematical model and corresponding numerical method to describe inclined settling coupled with natural convection. The model consists in a two-dimensional scalar conservation law for the solids concentration coupled with a version of the Stokes system that accounts for density fluctuations in the mixture enhanced by a Boussinesq approximation of the effect of fluctuating temperature plus a convection-diffusion equation for heat transport and diffusion. The main outcome is a simulator that allows one to determine the effect of controllable parameters such as the initial concentration, difference of temperature, and angle of inclination on the progress of the solid-liquid separation. The Boycott effect [4] as well as the Boussinesq approximation have been studied widely; several mathematical models and numerical schemes for the approximate solution of both have been proposed. Nevertheless, and to point out the main novelty of the work, a numerical scheme that would allow the coupling between both systems has not been proposed so far. That said, we mention that also the solid concentration of the mixture influences its capacity of heat conduction and diffusion, a property that needs to be taken into account for various solid materials. In fact, heat should be applied moderately only to avoid influencing the process excessively or even causing damage to the equipment due to excessive heat.

1.2 Related work

In his famous note [4], Boycott reported that corpuscles blood settled more rapidly in inclined tubes than in vertical ones. He presented a number of rough experiments that differed in the dimensions and angle of inclination of the tube. Recognizing that both parameters influence the speed of production of liquid (clear serum) he asked for an explanation of the phenomenon. One of the first attempts to explain the phenomenon is due to Ponder [33] and later Nakamura and Kuroda [28] (see also [39,41]), who developed the so-called Ponder-Nakamura-Kuroda (PNK) theory that postulated that the settling rate of an initially homogeneous suspension would be determined by the settling velocity v_{settl} multiplied by the cross-sectional area of the vessel available for settling. However, the PNK theory produces an acceptable approximation only under idealizing assumptions, and mostly over-predicts the increase in settling rate, as is pointed out by Graham and Lama [22]. On the other hand, that work, as well as others of the 1960s and 1970s [1, 29, 32, 44], provide experimental support and partial theoretical explanations of the Boycott effect and underline the importance of the initial solids concentration on the settling velocity of particles.

The standard kinematic sedimentation theory by Kynch [24] postulates that the solid-fluid relative velocity $\boldsymbol{v}_{\mathrm{r}}$ in a monodisperse suspension of small rigid spheres is a function of local solids volume fraction ϕ such that $\boldsymbol{v}_{\mathrm{r}} = v_{\mathrm{r}}(\phi)\boldsymbol{k}$, where $\boldsymbol{k}$ is the unit vector pointing into the direction of gravity, and $v_{\mathrm{r}}(\phi)$ is a given constitutive function that should satisfy $v_{\mathrm{r}}(0) = 1$. It is well known that if we define $f_{\mathrm{bk}}(\phi) \coloneqq \phi(1-\phi)v_{\mathrm{r}}(\phi)$ and z to be the downward-increasing vertical spatial coordinate (depth), then one-dimensional settling of a monodisperse suspension in a cylindrical closed column can be described by the first-order nonlinear conservation law

$$\frac{\partial \phi}{\partial t} + \frac{\partial f_{\mathrm{bk}}(\phi)}{\partial z} = 0,$$

supplied with initial conditions [12–14]. (The kinematic theory gives rise to first-order quasilinear PDEs, also in the cases of extensions to polydisperse suspensions [6] and rotating systems [16].) The same theory is employed herein to describe the solid-liquid separation aligned with gravity. A common choice of the function $v_{\mathrm{r}}(\phi)$ is due to Richardson and Zaki [36], namely

$$v_{\mathrm{r}}(\phi) = v_0(1-\phi)^{n_{\mathrm{RZ}}-1}, \quad \text{hence} \quad f_{\mathrm{bk}}(\phi) = v_0\phi(1-\phi)^{n_{\mathrm{RZ}}}, \tag{1.1}$$

where v_0 is the Stokes velocity, that is the settling velocity of one particle in quiescent pure fluid, and $n_{\mathrm{RZ}} > 1$ is a material specific exponent. The equation for $f_{\mathrm{bk}}(\phi)$ can also be written in terms of the hindered settling velocity v_{hs} such that $f_{\mathrm{bk}}(\phi) = \phi v_{\mathrm{hs}}(\phi)$. For choices of $f_{\mathrm{bk}}(\phi)$ alternative to (1.1) and methods of obtaining this function from experiments we refer to [5].

With respect to mathematical models, we mention that based on their previous work [26], McCaffery et al. [27] formulate a two-dimensional model to predict the behaviour of solid particles in an inclined channel during hydraulic separation. On the other hand, Bürger et al. [11] derive spatially multi-dimensional model equations for sedimentation-consolidation processes. Their approach is based on the mass and linear momentum balance equations for the solid and liquid phases, introducing constitutive assumptions, and applying a dimensional analysis. Specific computational methods applied to the simulation of the Boycott effect include the works by Latsa et al. [25], who employ upwind schemes to simulate sedimentation in inclined tanks; Wan [43] who advances a finite element-finite volume method for the simulation of two immiscible fluids; and Kleine and Reddy [23] who develop a κ-ε-type finite element method to conserve the mass of the system. On the other hand, McCaffery et al. [27] employ a Godunov-type finite volume (FV) scheme coupled with a particular control volume method [31]. Based on a FV method including a pressure stabilization technique for the Stokes problem coupled with the mentioned Godunov scheme for the

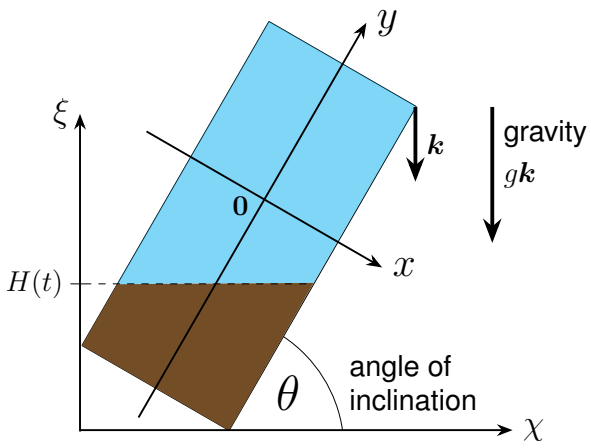

FIGURE 2. Schematic of PNK theory. Inclination angle $\theta \in (0, \pi/2]$ is measured with respect to the horizontal axis and vector $\boldsymbol{k} = (\cos(\theta), -\sin(\theta))^{\mathtt{t}}$ is pointing in the direction of gravity. Axes x and y are relative to the domain as indicated in the image.

concentration equation, Bürger et al. [8] solve the model equations by an adaptive multiresolution method. For a related model including sediment compressibility, which makes the concentration equation degenerate parabolic (cf., e.g., [7, 10]), Bürger et al. [9] propose a stabilized finite volume element (FVE) method while Ruiz-Baier and Lunati [37] present a discontinuous FVE method.

A classical reference to the phenomenon of convection is Ostrach [30], who underlines the extremely complex nature of the problem of natural convection in cavities due to the large number of parameters involved. More recent numerical studies related to the phenomenon of natural convection include Christon et al. [17] who also review solutions found in the literature to critical parameters for the occurrence of instability of a differentially heated, vertical cavity, while Dou et al. [19] simulate the convection process with the difference that in their case, the fluid container is inclined. Our approach has in particular been motivated by the treatment by Reyes et al. [35] who study the heat-assisted sedimentation of suspensions of mineral particles in inclined vessels. To this end they use simulations by OpenFoam in two space dimensions for various operating conditions.

1.3 Outline of the paper

The remainder of this work is organized as follows. In Section 2 we provide the theoretical framework, starting in Section 2.1 with a general description of the settling process. Next, in Section 2.2 we review in some detail the descriptions of inclined settling by PNK theory [28, 33] and McCaffery et al. [27]. The governing equations of the present approach are formulated in Section 2.3. Roughly speaking, our model is consistent with that by McCaffery et al. [27] (who treat the iso-thermal case). However, our equation of motion of the mixture does not include an advective acceleration term, but does include temperature- and concentration-dependent mixture viscosity, a Boussinesq approximation to the dependence of density on temperature, and of course the model includes a heat convection-diffusion equation. In Section 3 the numerical scheme is introduced. After stating some preliminaries in Section 3.1, in particular the Cartesian mesh of control volumes and "ghost cells," we introduce the three building blocks of the discretization of the governing equations, namely FV schemes for the approximation of the concentration equation (Section 3.2), the Stokes system (Section 3.3), and the heat equation (Section 3.4). In Section 3.5

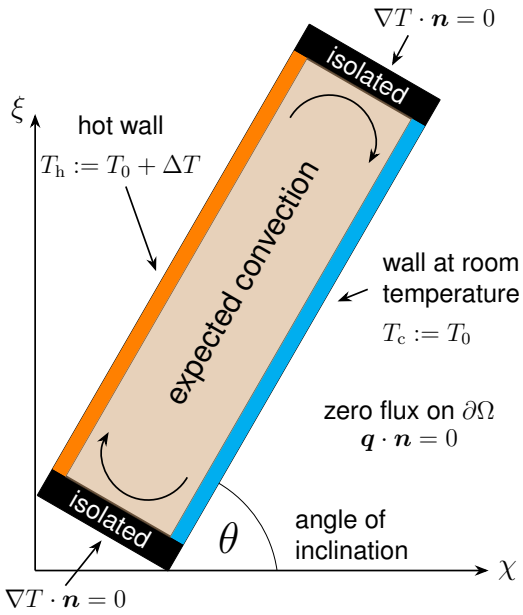

FIGURE 3. Initial and boundary conditions and schematic of the phenomenon of natural convection. Here T_0 is the initial and cold (right) wall temperature, and T_h is the temperature at the hot (left) wall, with $\Delta T \geq 0$. The top and bottom walls are assumed to be isolated.

we specify the Courant-Friedrichs-Lewy (CFL) condition for the explicitly solved concentration and heat equations, that is the bound of the time step in terms of the spatial meshwidths so that the scheme behaves stably. The schemes outlined in Sections 3.2 to 3.4 are combined by a strategy to handle the fully coupled model, as is outlined in Section 3.6, see Algorithm 1. In Section 4 we present numerical simulations of the inclined sedimentation process with natural convection for various cases of interest. Simulation 1 (Section 4.1) addresses the so-called Diehl test that is based on studying the behaviour of the mixture when a body of concentrated suspension is initially located above clear liquid. This configuration is of interest to solve the inverse problem of flux identification from experimental data [5,18]. In Simulation 2 (Section 4.2) we compare the results of simulations of two different combinations of the temperature variation (due to heating) and coefficients of thermal expansion. In Simulation 3 (Section 4.3) we simulate settling in inclined vessels under systematic variation of the angle of inclination. The parameters are chosen as typical for applications in mineral processing. However, the increase of rates of production of clear liquid and sediment formation under heating turns out to be at most marginal compared with corresponding inclined configurations without heating. A slight increase can, however, be observed if we assume that the solid-fluid density is relatively small, as is documented in Simulation 4 (Section 4.4). Conclusions of the study are collected in Section 5.

2 Theoretical framework

2.1 Description of the settling process

The sedimentation process, thickening or clarification, consists of the operation of separating part of the liquid from a suspension to obtain a flow of clear water or purer liquid and, on the other hand, denser matter obtained from the suspension. The mechanism considered in this work is sedimentation by gravity, in which solid particles settle downward to the bottom of the vessel or container. In the wastewater and mining industry, the vessel in which the sedimentation process is carried out is called settler or tank. In our examples, the tank is composed of two thermally isolated walls and two walls exposed to heating sources, for which one of them is assumed to have a constant temperature (room temperature) and the other one is at a higher temperature. The tank is assumed to have constant depth so that a two-dimensional description is appropriate with a length to width aspect ratio 4:1, and an angle of inclination θ with respect to the horizontal, see Figure 3.

2.2 Inclined settling

The Ponder-Nakamura-Kuroda (PNK) theory [28, 33, 39, 41] postulates that the increase in settling rate in an inclined vessel is due to the increase of horizontal settling area due to the inclination of the channel (compared with a vertical orientation). Within the PNK theory, the rate of descent $U(t)$ of the clear liquid/suspension interface is determined by

$$U(t) = v_{\mathrm{hs}}(\phi)\left(\frac{b}{\sin\theta} + H(t)\cot\theta\right),$$

where v_{hs} is the given hindered settling velocity obtained from the vertical theory, b is the width of the vessel, θ is its angle of inclination with respect to the horizontal axis and $H(t)$ is the height of the interface at time t, see Figure 2. It is well known that PNK theory produces an acceptable approximation only under idealizing assumptions, and mostly over-predicts the increase in settling rate. In fact, a simple one-dimensional kinematic model is not adequate for the description of settling in an inclined vessel; rather, a coupled transport-flow model is needed. One model of that kind was studied by McCaffery et al. [27]. It can be described by the transport equation

$$\frac{\partial\phi}{\partial t} + \operatorname{div}\big(\phi\boldsymbol{q} + \phi v_{\mathrm{hs}}(\phi)\boldsymbol{k}\big) = 0, \tag{2.1}$$

where $\boldsymbol{q}$ is the volume average velocity of the mixture and $\boldsymbol{k}$ is the downward-pointing unit vector (aligned with gravity), coupled to the version of the Stokes system

$$-\mathbf{div}\big(2\mu(\phi)\boldsymbol{e}(\boldsymbol{q})\big) + \lambda\nabla p = \lambda\Delta\rho^*\phi\boldsymbol{k}, \tag{2.2}$$

$$\operatorname{div}\boldsymbol{q} = 0, \tag{2.3}$$

where $\mu(\phi)$ is the (concentration-dependent) viscosity of the mixture, $\boldsymbol{e}(\boldsymbol{q}) := \frac{1}{2}(\nabla\boldsymbol{q} + (\nabla\boldsymbol{q})^{\mathrm{T}})$ is the symmetric part of the gradient of $\boldsymbol{q}$, and

$$\Delta\rho^* := \frac{\rho_{\mathrm{s}} - \rho_{\mathrm{f}}}{\rho_{\mathrm{f}}}, \quad \lambda := \frac{D^2 g\rho_{\mathrm{f}}}{v_0\mu_{\mathrm{f}}}, \tag{2.4}$$

are non-dimensional parameters, where D is the characteristic length of the problem. Equation (2.1) expresses the conservation of mass of the solid component while (2.2) and (2.3) represent the conservation of linear momentum and of mass of the mixture, respectively. The sought unknowns in (2.1)–(2.3) are the solids volume fraction ϕ, the velocity $\boldsymbol{q}$ and the pressure p, all functions of

spatial position $\boldsymbol{x}$ and time t. Notice that (2.1)–(2.3) stipulates a strong ("two-way") coupling between the unknowns: on one hand, the solution of (2.1) depends on the local behaviour of $\boldsymbol{q}$ due to the transport term $\phi\boldsymbol{q}$, and the velocity field $\boldsymbol{q}$, in turn, depends on the local fluctuations of concentration through the variable viscosity and the right-hand side in (2.2). The strategy in [27] to approximate the nonlinear part of (2.1) was based on the Godunov numerical flux, while a FV scheme is employed for the flow equations (2.2) and (2.3). Bürger et al. [8] enhanced the numerical results of [27] by using a multiresolution FV scheme. In the same line, Ruiz-Baier and Torres [38] used a scheme based on FVE methods and studied inclined sedimentation. They included in Equation (2.2) the additional convective term $\partial_t\boldsymbol{q} + \boldsymbol{q}\cdot\nabla\boldsymbol{q}$, obtaining fully transient model equations.

2.3 Governing equations

In addition to the classic two-phase sedimentation process, we take into account the phenomenon of natural convection in cavities (cf., e.g., [2, 17, 40], and references cited in these works). In this phenomenon, the movement of the fluid is produced by the difference in density generated by modifying the temperature of parts of the vessel that contain the suspension (see Figure 3).

Under the Boussinesq approximation, we may assume the density of the mixture ρ depends on the temperature of the mixture denoted by T, this is, $\rho(T) = \rho_0 - \beta\rho_0(T - T_0)$, where

$$\beta = -\frac{1}{\rho_0}\frac{\partial\rho}{\partial T}$$

and $\rho_0 = \rho(T_0)$, where T_0 is a reference temperature. These assumptions lead to the modified momentum balance and energy equations (see for instance [3])

$$\rho_0\left(\frac{\partial\boldsymbol{q}}{\partial t} + \boldsymbol{q}\cdot\nabla\boldsymbol{q}\right) - \mathbf{div}\big(2\mu(\phi)\boldsymbol{e}(\boldsymbol{q})\big) + \nabla p = \rho_0 g\boldsymbol{k} - \rho_0 g\boldsymbol{k}\beta(T - T_0),$$

$$\rho_0 c_{\mathrm{p}}\left(\frac{\partial T}{\partial t} + \boldsymbol{q}\cdot\nabla T\right) - \kappa\,\mathrm{div}(\nabla T) = 0,$$

where κ is the conduction heat transfer coefficient and c_{p} is the heat capacity of the fluid.

Sedimentation in inclined vessels coupled with natural convection was studied by Reyes et al. [34], where the governing equations given by the conservation equations of mass, momentum and internal energy for the liquid and solid phase are solved using the computational fluid mechanics software Open Foam. The momentum balance and energy equations utilized in [34] are

$$\rho(\phi)\left(\frac{\partial\boldsymbol{q}}{\partial t} + \boldsymbol{q}\cdot\nabla\boldsymbol{q}\right) - \mathbf{div}\left(2\mu(\phi,T)\boldsymbol{e}(\boldsymbol{q})\right) + \nabla p = \rho(\phi,T)g\boldsymbol{k},$$

$$\rho(\phi)c_{\mathrm{p}}(\phi)\left(\frac{\partial T}{\partial t} + \boldsymbol{q}\cdot\nabla T\right) - \kappa(\phi)\,\mathrm{div}(\nabla T) = 0.$$

Note that c_{p} and κ depend on the solids volume fraction ϕ, while μ and ρ depend on temperature T and volume fraction ϕ. The Boussinesq approximation in this case is applied to ρ as

$$\begin{aligned}\rho(\phi,T) &= \rho(\phi) + \frac{\partial\rho(\phi,T_0)}{\partial T}(T - T_0) = \rho(\phi) + \frac{\partial(\phi\rho_{\mathrm{s}} + (1-\phi)\rho_{\mathrm{f}})}{\partial T}(T - T_0)\\ &= \rho(\phi) + (1-\phi)\frac{\partial\rho_{\mathrm{f}}}{\partial T}(T - T_0) = \rho(\phi) - (1-\phi)\rho_{\mathrm{f}}\beta_{\mathrm{f}}(T - T_0),\end{aligned} \tag{2.5}$$

where β_{f} is the coefficient of thermal expansion of the fluid phase. In (2.5) the corresponding coefficient of thermal expansion of the solid phase has been neglected. Then, following the dimensional

analysis of [11] as well as Unwin [42], we omit the material derivative in the momentum balance. Thus the final system of governing equations becomes

$$\begin{aligned} \frac{\partial \phi}{\partial t} + \operatorname{div}\big(\boldsymbol{q}\phi + \phi v_{\mathrm{hs}}(\phi)\boldsymbol{k}\big) &= 0, \\ -\mathbf{div}\left(2\mu(\phi,T)\boldsymbol{e}(\boldsymbol{q})\right) + \nabla p &= \rho(\phi)\boldsymbol{k} - (1-\phi)\beta_{\mathrm{f}}(T-T_0)\boldsymbol{k}, \\ \operatorname{div}\boldsymbol{q} &= 0, \\ \rho(\phi)c_{\mathrm{p}}(\phi)\left(\frac{\partial T}{\partial t} + \boldsymbol{q}\cdot\nabla T\right) - \kappa(\phi)\operatorname{div}(\nabla T) &= 0. \end{aligned} \tag{2.6}$$

These are three scalar equations plus one vector equation and five unknowns, namely the solids volume fraction ϕ, the volume-average velocity $\boldsymbol{q}$, pressure p and temperature T. This system is closed by the constitutive relations

$$\begin{aligned} v_{\mathrm{hs}} = v_{\mathrm{hs}}(\phi) &= v_0(1-\phi)^{n_{\mathrm{RZ}}}, \\ \mu = \mu(\phi) &= \mu_{\mathrm{f}}(1-\phi)^{-\alpha}, \quad \alpha \geq 0, \\ \kappa = \kappa(\phi) &= \kappa_{\mathrm{f}}(1-\phi) + \kappa_{\mathrm{s}}\phi, \\ c_{\mathrm{p}} = c_{\mathrm{p}}(\phi) &= c_{p_{\mathrm{f}}}(1-\phi) + c_{p_{\mathrm{s}}}\phi. \end{aligned} \tag{2.7}$$

To formulate the dimensionless version of (2.6), we introduce dimensionless variables and functions

$$\begin{aligned} &\boldsymbol{x} = \boldsymbol{x}^* L, \quad \boldsymbol{q} = \boldsymbol{q}^* v_0, \quad T = T^*\Delta T + T_0, \quad t = \frac{L}{v_0}t^*, \quad \nabla^* = L\nabla, \quad \frac{\partial}{\partial t} = \frac{v_0}{L}\frac{\partial}{\partial t^*}, \\ &\rho = \rho_{\mathrm{f}}\rho^*, \quad \kappa = \kappa_{\mathrm{f}}\kappa^*, \quad c_{\mathrm{p}} = c_{p_{\mathrm{f}}}c_{\mathrm{p}}^*, \quad p = \rho g L(p^* + \boldsymbol{k}\cdot\boldsymbol{x}^*), \end{aligned}$$

where L is the characteristic length of the domain, the subscript 'f' indicates fluid and an asterisk denotes the corresponding dimensionless variable. We also define additional functions

$$\begin{aligned} \boldsymbol{f}^*(\phi,T^*) &\coloneqq \lambda\Delta\rho^*\phi\boldsymbol{k} - \lambda(1-\phi)\beta_{\mathrm{f}}T^*\Delta T\boldsymbol{k}, \\ \tilde{\kappa}^*(\phi) &\coloneqq \frac{\mu_{\mathrm{f}}}{\rho_{\mathrm{f}}v_0 L\,\mathrm{Pr}}\frac{(1+\phi\Delta\kappa^*)}{(1+\phi\Delta c_{\mathrm{p}}^*)\,(1+\phi\Delta\rho^*)}. \end{aligned} \tag{2.8}$$

For ease of notation, we drop the asterisk and directly write the dimensionless version of (2.6) as

$$\frac{\partial \phi}{\partial t} + \operatorname{div}\big(\boldsymbol{q}\phi + \phi v_{\mathrm{hs}}(\phi)\boldsymbol{k}\big) = 0, \tag{2.9a}$$

$$-\mathbf{div}\big(2\mu(\phi)\boldsymbol{e}(\boldsymbol{q})\big) + \lambda\nabla p = \boldsymbol{f}(\phi,T), \tag{2.9b}$$

$$\operatorname{div}\boldsymbol{q} = 0, \tag{2.9c}$$

$$\frac{\partial T}{\partial t} + \boldsymbol{q}\cdot\nabla T = \tilde{\kappa}(\phi)\operatorname{div}(\nabla T)\,. \tag{2.9d}$$

The dimensionless parameters $\Delta\rho^*$ and λ, which are also introduced in [27], are defined in (2.4) (with the characteristic length D replaced by L). Typical values in mineral processing are [11]:

$$\begin{aligned} &v_0 = 10^{-4}\,\mathrm{m/s}, \quad \nu_{\mathrm{f}} = 10^{-6}, \quad \mu_{\mathrm{f}} = 10^{-4}\,\mathrm{Pa\,s}, \\ &g = 10\,\mathrm{m/s^2}, \quad \mathrm{Pr} = 7, \quad L = 1\,\mathrm{m}, \quad \mathrm{Re} = 10^{-2}. \end{aligned} \tag{2.10}$$

In what follows the dimensionless equations (2.9) are assumed to be in effect.

The velocity equation is complemented with zero-flux boundary conditions:

$$\boldsymbol{q}\cdot\boldsymbol{n} = 0 \quad \text{on } \partial\Omega. \tag{2.11}$$

Regarding the mass equation, we will initially consider a constant and uniform density throughout the domain,

$$\phi(\boldsymbol{x},0)=\phi_0 \quad \text{for all } \boldsymbol{x}\in\Omega \tag{2.12}$$

in addition to zero flux boundary conditions, i.e., $(\phi\boldsymbol{q}+\phi v_{\mathrm{hs}}(\phi)\boldsymbol{k})\cdot\boldsymbol{n}=0$ on $\partial\Omega$. In light of (2.11) this condition reduces to

$$\big(\phi v_{\mathrm{hs}}(\phi)\boldsymbol{k}\big)\cdot\boldsymbol{n}=0 \quad \text{on } \partial\Omega. \tag{2.13}$$

Finally, for the heat equation, we impose the constant initial temperature

$$T(\boldsymbol{x},0)=T_0 \quad \text{for all } \boldsymbol{x}\in\Omega \tag{2.14}$$

and Dirichlet boundary conditions on the left and right walls are given by T_{h} (hot wall) and T_0 (cold wall), respectively, and zero flux boundary conditions for the top and bottom walls, that is

$$T(x_{\mathrm{a}},y,t)=T_{\mathrm{h}}, \quad T(x_{\mathrm{b}},y,t)=T_0 \quad \text{for all } y\in(0,4L),\ t>0; \tag{2.15}$$

$$(\boldsymbol{n}\cdot\nabla T)(x,y_{\mathrm{a}},t)=(\boldsymbol{n}\cdot\nabla T)(x,y_{\mathrm{b}},t)=0 \quad \text{for all } x\in(0,L),\ t>0. \tag{2.16}$$

(In the non-dimensional case, T_{h} and T_0 in (2.15) need to be replaced by one and zero, respectively.) Finally, the following assumptions are made to ensure that the model is physically and mathematically reasonable.

3 Numerical scheme

3.1 Preliminaries

To numerically solve system (2.9), we discretize Ω by $N_x\cdot N_y$ square control volumes of constant size $\Delta x\times\Delta y$, which form a mesh $\mathcal{T}$ that satisfies all the assumptions of an admissible mesh given in [20]. Since Ω is rectangular, $x_{\mathrm{a}}\le x\le x_{\mathrm{b}}$ and $y_{\mathrm{a}}\le y\le y_{\mathrm{b}}$ with $x_{\mathrm{a}}<x_{\mathrm{b}}$ and $y_{\mathrm{a}}<y_{\mathrm{b}}$, i.e., the left-bottom corner of Ω is $(x_{\mathrm{a}},y_{\mathrm{a}})$. Each cell or control volume is then given by $[x_{i-1/2},x_{i+1/2}]\times[y_{j-1/2},y_{j+1/2}]$ with $x_{i+1/2}\coloneqq x_{\mathrm{a}}+i\Delta x$ and $y_{j+1/2}\coloneqq y_{\mathrm{a}}+j\Delta y$ for $i=0,1,\dots,N_x$ and $j=0,1,\dots,N_y$. The center of a control volume $K_{i,j}\in\mathcal{T}$ is

$$\boldsymbol{x}_{K_{i,j}}\coloneqq(x_i,y_j)\coloneqq\big(x_{\mathrm{a}}+(i-\tfrac{1}{2})\Delta x,y_{\mathrm{a}}+(j-\tfrac{1}{2})\Delta y\big).$$

We approximate all unknowns as piecewise constant functions over every control volume in $\mathcal{T}$. Furthermore, in order to impose the boundary conditions, extra control volumes or ghost cells are incorporated next to each one of the straight boundaries of the domain. Figure 4 illustrates the squared control volumes and the so-called ghost cells near the boundary at $x=x_{\mathrm{b}}$. During the course of this section, $K\in\mathcal{T}$ (without indices) is assumed to be a generic control volume and $\sigma=K|K^*$ the edge of K shared with its neighbour control volume $K^*\in\mathcal{T}$. In addition, we define $\mathcal{E}$ as the set of edges related to $\mathcal{T}$, m_σ as the measure of the edge $\sigma\in\mathcal{E}$, and $\boldsymbol{n}_{K,\sigma}$ as the unit normal vector at σ pointing outward to K. Furthermore, we define $d_{K|K^*}\coloneqq\|\boldsymbol{x}_{K^*}-\boldsymbol{x}_K\|$ and $\tau_\sigma\coloneqq m_\sigma/d_\sigma$.

The set of edges of K is denoted by $\mathcal{E}_K$, and the set of interior and exterior edges (with respect to the boundary $\partial\Omega$) are denoted by $\mathcal{E}_{\mathrm{int}}$ and $\mathcal{E}_{\mathrm{ext}}$, respectively. The set of neighbouring control volumes to K is defined as $\mathcal{N}_K$ and m_K denotes the measure of K. In addition, we define $H_{\mathcal{T}}(\Omega)\subset L^2(\Omega)$ as the space of piecewise constant functions on each control volume of $\mathcal{T}$, this is

$$H_{\mathcal{T}}(\Omega)\coloneqq\big\{w\in L^2(\Omega):\quad w|_K\equiv k\in\mathbb{R},\quad \forall K\in\mathcal{T}\big\}.$$

Here, for all $w\in H_{\mathcal{T}}(\Omega)$ and $K\in\mathcal{T}$, the restriction of w to K is denoted by w_K, and $L^2(\Omega)$ is the

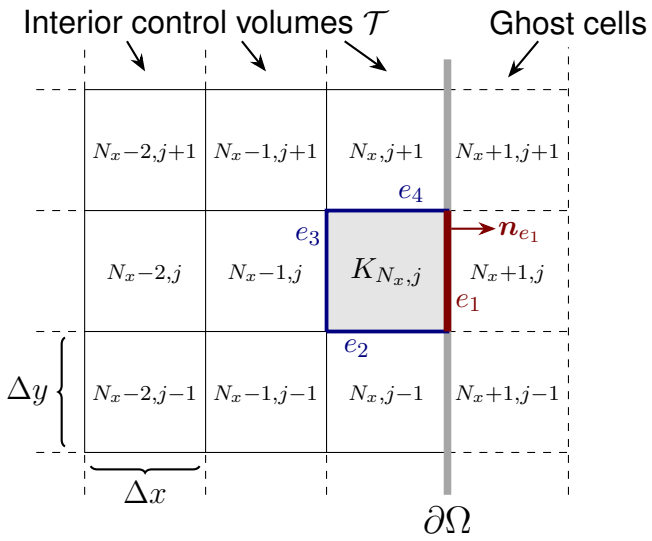

FIGURE 4. Illustration of control volumes near the right boundary at $x = x_\mathrm{b}$ and neighbouring ghost cells. Boundary edges of $K_{N_x,j}$ are such that $e_1 \in \mathcal{E}_\mathrm{ext}$ and $e_2, e_3, e_4 \in \mathcal{E}_\mathrm{int}$.

space of square-integrable functions over Ω. Finally, we introduce the upwind operator for a given velocity $v \in \mathbb{R}$

$$\mathrm{Upw}(v; a, b) \coloneqq \max\{v, 0\}a + \min\{v, 0\}b \quad \text{for all } a, b, c \in \mathbb{R}.$$

In the remainder of this section, to refer to variables or functions restricted to a control volume $K = K_{i,j}$ we use both types of notations, i.e., $\phi_{i,j} \equiv \phi_K$.

3.2 Approximation of the concentration equation

We discretize (2.9a) by a FV scheme. We denote by

$$\bar{\phi}_K \coloneqq \frac{1}{m_K}\int_K \phi(x,t)\,\mathrm{d}\boldsymbol{x}, \quad \text{where} \quad m_K \coloneqq \int_K \mathrm{d}\boldsymbol{x} = \Delta x \Delta y,$$

the cell average of ϕ on the control volume K at time $t > 0$. In addition, we define $\bar{\phi}_K^n \coloneqq \bar{\phi}_K(t_n)$, where $t_n = n\Delta t$ for $n \in \mathbb{N}$ and $\Delta t > 0$ is a time step specified later. To discretize the solid mass balance equation (2.9a) we rewrite this equation as

$$\frac{\partial \phi}{\partial t} + \operatorname{div} \boldsymbol{F}(\boldsymbol{q}, \phi) = \frac{\partial \phi}{\partial t} + \frac{\partial F^x}{\partial x} + \frac{\partial F^y}{\partial y} = 0, \tag{3.1}$$

where the x- and y- components of the flux vector $\boldsymbol{F}$ are given by

$$F^x(q^x, \phi) \coloneqq \phi q^x + \phi v_\mathrm{hs}(\phi)\cos\theta \quad \text{and} \quad F^y(q^y, \phi) \coloneqq \phi q^y - \phi v_\mathrm{hs}(\phi)\sin\theta, \tag{3.2}$$

respectively. The fluxes F^x and F^y are approximated on cell boundaries by combining the Godunov numerical flux [21] with an upwind flux. Equation (3.1) is then discretized by a fractional stepping method: in the first step, the solution is updated in the x-direction, i.e., we compute

$$\phi_{i,j}^{n+1/2} = \phi_{i,j}^n - \frac{\Delta t}{\Delta x}\big(F_{i+1/2,j}^{x,n} - F_{i-1/2,j}^{x,n}\big), \tag{3.3}$$

and then, using these intermediate variables indexed with $n+1/2$, one updates the solution in the y-direction and therefore computes the updated solution at time t_{n+1} by

$$\phi_{i,j}^{n+1} = \phi_{i,j}^{n+1/2} - \frac{\Delta t}{\Delta y}\big(F_{i,j+1/2}^{y,n} - F_{i,j-1/2}^{y,n}\big). \tag{3.4}$$

The numerical fluxes $F_{i+1/2,j}^{x}$ and $F_{i,j+1/2}^{y}$ are defined by

$$\begin{aligned} F_{i+1/2,j}^{x,n} &\coloneqq \mathrm{Upw}\big((q_{i,j}^{x,n} + q_{i+1,j}^{x,n})/2; \phi_{i,j}^{n}, \phi_{i+1,j}^{n}\big) + G\big(\phi_{i,j}^{n}, \phi_{i+1,j}^{n}\big)\cos\theta, \\ F_{i,j+1/2}^{y,n} &\coloneqq \mathrm{Upw}\big((q_{i,j}^{y,n} + q_{i,j+1}^{y,n})/2; \phi_{i,j}^{n+1/2}, \phi_{i,j+1}^{n+1/2}\big) - G\big(\phi_{i,j+1}^{n+1/2}, \phi_{i,j}^{n+1/2}\big)\sin\theta \end{aligned} \tag{3.5}$$

for all $i = 0, 1, \ldots, N_x$ and $j = 0, 1, \ldots, N_y$, where the velocity terms at the cell boundaries are given by the averages and the Godunov numerical flux G for a flux density function f is given by

$$G(a,b) \coloneqq \begin{cases} \min\limits_{a \le \phi \le b} f(\phi) & \text{if } a \le b, \\ \max\limits_{a \ge \phi \ge b} f(\phi) & \text{if } a \ge b. \end{cases} \tag{3.6}$$

Notice that the evaluation of the right-hand side of (3.6) requires knowledge of the local extrema of the function f. In the case of the functions F^x and F^y these extrema depend on the values of q^x and q^y, which in turn vary in each cell and are part of the computation. This would make the approximation of all terms in F^x and F^y through the Godunov numerical flux inconvenient. However, if f is a function with exactly one maximum at $\hat{\phi} \in (0,1)$, then (3.6) implies that

$$G(a,b) = \min\big\{f(\min\{a,\hat{\phi}\}), f(\max\{b,\hat{\phi}\})\big\} \quad \text{for all } a, b \in \mathbb{R}^+,$$

so $G(a,b)$ can be evaluated easily, which motivates the "upwind plus Godunov" definition of numerical fluxes (3.5).

The zero-flux boundary conditions (2.11) and (2.13) ensure that there is no loss or gain of mass within the domain. A concentration value of $\phi = 1$ is assigned to the ghost cells that share an edge with the boundary cells with normal pointing towards the ground directions at each cell boundary a, and the rest of the ghost cells are assigned a concentration value $\phi = 0$. In other words, to impose (2.13), Dirichlet boundary conditions are imposed on each one of the boundary edges of $\partial\Omega$.

3.3 Approximation of the Stokes system

The system composed of (2.9b) and (2.9c) for the velocity field $\boldsymbol{q}$ and pressure p has the structure of the Stokes system. The discrete gradient of $w \in H_{\mathcal{T}}$ on $K \in \mathcal{T}$ is computed by differences between w_K and the values of w on each control volume adjacent to K. Then, we define the discrete gradient operator as $\nabla_{\mathcal{T}} : H_{\mathcal{T}}(\Omega) \to [H_{\mathcal{T}}(\Omega)]^d$ such that

$$(\nabla_{\mathcal{T}} w)_K \coloneqq \frac{1}{m_K} \sum_{L \in \mathcal{N}_K} \frac{m_{K|L}}{d_{K|L}} \frac{x_L - x_K}{2}(w_L - w_K) \quad \text{for all } w \in H_{\mathcal{T}}(\Omega) \text{ and } K \in \mathcal{T}. \tag{3.7}$$

The adjoint operator of the discrete gradient given in (3.7) defines the discrete divergence acting on vector functions $\mathrm{div}_{\mathcal{T}} : [H_{\mathcal{T}}(\Omega)]^d \to H_{\mathcal{T}}(\Omega)$ such that

$$\mathrm{div}_{\mathcal{T}}(\boldsymbol{w})(x) \coloneqq \frac{1}{m_K} \sum_{L \in \mathcal{N}_K} \frac{m_{K|L}}{d_{K|L}} \frac{\boldsymbol{x}_L - \boldsymbol{x}_K}{2} \cdot (\boldsymbol{w}_K + \boldsymbol{w}_L) \quad \text{for all } \boldsymbol{w} \in [H_{\mathcal{T}}(\Omega)]^d \text{ and } K \in \mathcal{T}. \tag{3.8}$$

The specific definitions of the discrete operators (3.7) and (3.8) ensure that for every pair $(v, w) \in (H_{\mathcal{T}}(\Omega))^2$, the inner product

$$\langle v, w\rangle_{\mathcal{T}} = \frac{1}{2}\sum_{K\in\mathcal{T}}\sum_{L\in\mathcal{N}_K}\frac{m_{K|L}}{d_{K|L}}(v_L - v_K)(w_L - w_K) \tag{3.9}$$

in line with Neumann boundary conditions and the corresponding inner product

$$[v, w]_{\mathcal{T}} = \langle v, w\rangle_{\mathcal{T}} + \sum_{K\in\mathcal{T}}\sum_{\sigma\in\mathcal{E}_K\cap\mathcal{E}_{\text{ext}}}\frac{m_\sigma}{d_{K,\sigma}}v_K w_K \tag{3.10}$$

related to Dirichlet boundary conditions are well defined. Moreover, since we assume variable viscosity $\mu = \mu(\phi)$, we include $\mu(\phi)$ as a weight function in the inner products. Consequently, (3.9) and (3.10) are replaced by

$$\langle v, w\rangle_{\mathcal{T},\mu} \coloneqq \frac{1}{2}\sum_{K\in\mathcal{T}}\sum_{L\in\mathcal{N}_K}\frac{m_{K|L}}{d_{K|L}(\mu_K + \mu_L)}(v_L - v_K)(w_L - w_K),$$

$$[v, w]_{\mathcal{T},\mu} \coloneqq \langle v, w\rangle_{\mathcal{T},\mu} + \sum_{K\in\mathcal{T}}\sum_{\sigma\in\mathcal{E}_K\cap\mathcal{E}_{\text{ext}}}\frac{m_\sigma}{d_{K,\sigma}}\mu_K v_K w_K.$$

A stabilized method for the pressure is defined by following the treatment of [8]. An additional term $\eta^2\Delta p$ is introduced to modify the continuity equation (2.9c), where $\eta > 0$ is a regularization parameter. Then, assuming that $\mu(\phi) > 0$ and $\boldsymbol{f} \in [L^2(\Omega)]^2$, we consider the following perturbation of the Stokes system (2.9b), (2.9c):

$$\begin{aligned} -\mathbf{div}\big(\mu(\phi)\nabla\boldsymbol{q}^\eta\big) + \lambda\nabla p^\eta &= \boldsymbol{f}(\phi, T) && \text{in } \Omega\subset\mathbb{R}^2,\\ \nabla\cdot\boldsymbol{q}^\eta &= \eta^2\Delta p^\eta && \text{in } \Omega\subset\mathbb{R}^2,\\ \boldsymbol{q}^\eta &= 0 && \text{on } \partial\Omega, \end{aligned} \tag{3.11}$$

where $\boldsymbol{q}^\eta$ and p^η denote perturbed solutions with respect to the original unknowns $\boldsymbol{q}$ and p, respectively. We remark that for bounded values of p^η, the divergence of $\boldsymbol{q}^\eta$ tends to zero as η tends to zero. The system (3.11) has the same structure as part of the problem studied in [15] with η playing the role of $\xi(\phi)$. Therefore the analysis of [15] shows that (3.11) possesses unique solutions $\boldsymbol{q} \in [L^2(\Omega)]^2$ and $p \in L^2(\Omega)$. The weak formulation of (3.11) on the mesh $\mathcal{T}$ consists in finding $\boldsymbol{q} \in E_{\mathcal{T}}(\Omega), p \in H_{\mathcal{T}}(\Omega)$, with p of zero measure in Ω such that

$$\begin{aligned} [\boldsymbol{q}, \boldsymbol{u}]_{\mathcal{T},\mu} - \lambda\int_\Omega p(\boldsymbol{x})\,\mathrm{div}_{\mathcal{T}}\,\boldsymbol{u}(\boldsymbol{x})\,\mathrm{d}\boldsymbol{x} &= \int_\Omega \boldsymbol{f}(\phi, T)\cdot\boldsymbol{u}(\boldsymbol{x})\,\mathrm{d}\boldsymbol{x} && \text{for all } \boldsymbol{u}\in[H_{\mathcal{T}}(\Omega)]^2,\\ \int_\Omega \mathrm{div}_{\mathcal{T}}\,\boldsymbol{q}(\boldsymbol{x})q(\boldsymbol{x})\,\mathrm{d}\boldsymbol{x} &= -\eta^2\langle p, q\rangle_{\mathcal{T}} && \text{for all } q\in H_{\mathcal{T}}(\Omega). \end{aligned} \tag{3.12}$$

(We have dropped the superscript η although the variables correspond to the perturbed equation.) The parameter η must be adjusted to balance the accuracy and stability of the system. Then, after an integration by parts on each control volume $K \in \mathcal{T}$, system (3.12) is locally approximated by

$$\begin{aligned} \sum_{\sigma\in\mathcal{E}_K}\boldsymbol{S}^n_{K,\sigma} + \sum_{\sigma\in\mathcal{E}^{\text{int}}_K}\lambda(m_\sigma/2)\boldsymbol{n}_{K,\sigma}(p^n_{K^*} - p^n_K) &= \boldsymbol{f}(\phi^n_K, T^n_K),\\ \sum_{\sigma\in\mathcal{E}^{\text{int}}_K}(m_\sigma/2)\boldsymbol{n}_{K,\sigma}\cdot(\boldsymbol{q}^n_K + \boldsymbol{q}^n_{K^*}) - \sum_{\sigma\in\mathcal{E}^{\text{int}}_K}\eta^2\tau_\sigma(p^n_{K^*} - p^n_K) &= 0, \end{aligned} \tag{3.13}$$

where $\mathcal{E}_K^{\text{int}} \coloneqq \mathcal{E}_K \cap \mathcal{E}_{\text{int}}$, and for any control volume $K \in \mathcal{T}$ and interior edge $\sigma = K|K^*$ for $K^* \in \mathcal{T}$, the vector flux $\boldsymbol{S}_{K,\sigma}^n$ is defined as

$$\boldsymbol{S}_{K,\sigma}^n \coloneqq \frac{m_\sigma \mu_K^n \mu_{K^*}^n}{\mu_K^n d_{K,\sigma} + \mu_{K^*}^n d_{K^*,\sigma}} (\boldsymbol{q}_K^n - \boldsymbol{q}_{K^*}^n).$$

For an exterior edge $\sigma \in \mathcal{E}_{\text{ext}}$, we impose the zero-flux boundary condition (2.11) and define the flux vector on the boundary as

$$\boldsymbol{S}_{K,\sigma}^n \coloneqq \frac{m_\sigma \mu_K^n}{d_{K,\sigma}} \boldsymbol{q}_K^n.$$

The system (3.13) is supplemented with an additional condition of vanishing pressure average or incompressibility assumption on Ω, which serves as a uniqueness condition. This condition is incorporated into the linear system (3.13) through the equation

$$\sum_{K \in \mathcal{T}} m_K p_K^n = 0,$$

and the incorporation of an auxiliary unknown, augmenting the system by one row and one column.

3.4 Approximation of the heat equation

The heat equation (2.9d) is approximated by a semi-implicit scheme that is associated with a relaxed CFL condition (see Section 3.5) that avoids excessively small time steps due to the diffusion term in (2.9d). This semi-implicit scheme handles, in a first step, the transport part $\boldsymbol{q} \cdot \nabla T$ through an explicit discretization, and then in the second step, we include the diffusive part $\tilde{\kappa}(\phi) \operatorname{div}(\nabla T)$ by means of an implicit scheme. The transport part of (2.9d) is discretized via a splitting procedure to compute an intermediate solution, denoted by $T^{n+1/2}$, utilizing upwind numerical fluxes. Then, for each control volume $K_{i,j} \in \mathcal{T}$, we compute

$$T_{i,j}^{n+1/2} = T_{i,j}^n - \frac{\Delta t}{\Delta x} \big(U_{i+1/2,j}^{x,n} - U_{i-1/2,j}^{x,n} \big), \tag{3.14}$$

$$\tilde{T}_{i,j}^{n+1/2} = T_{i,j}^{n+1/2} - \frac{\Delta t}{\Delta y} \big(U_{i,j+1/2}^{y,n} - U_{i,j-1/2}^{y,n} \big), \tag{3.15}$$

where the convective numerical fluxes above are defined as

$$U_{i+1/2,j}^{x,n} \coloneqq \operatorname{Upw}\big((q_{i,j}^{x,n} + q_{i+1,j}^{x,n})/2; T_{i,j}^n, T_{i+1,j}^n \big) \quad \text{for } i \geq 0 \text{ and } j \geq 1,$$

$$U_{i,j+1/2}^{y,n} \coloneqq \operatorname{Upw}\big((q_{i,j}^{y,n} + q_{i,j+1}^{y,n})/2; T_{i,j}^{n+1/2}, T_{i,j+1}^{n+1/2} \big) \quad \text{for } i \geq 1 \text{ and } j \geq 0.$$

For the diffusive part, we observe that if ϕ is assumed to be piecewise constant, locally on a control volume $K \in \mathcal{T}$

$$\tilde{k}(\phi_K) \operatorname{div}(\nabla T_K) = \operatorname{div}\big(\tilde{k}(\phi_K) \nabla T_K \big).$$

Therefore, one way to approximate this term is to use the same scheme as for the viscous term in (3.11). Then for an interior edge $\sigma = K|K^* \in \mathcal{E}_{\text{int}}$, we define the diffusive flux as

$$\mathcal{D}_{K,\sigma}^n \coloneqq \frac{m_\sigma \tilde{\kappa}_K^n \tilde{\kappa}_{K^*}^n}{\tilde{\kappa}_K^n d_{K,\sigma} + \tilde{\kappa}_{K^*}^n d_{K^*,\sigma}} (T_K^n - T_{K^*}^n).$$

For the boundary edges in $\mathcal{E}^{\text{ext}}$, we need to take into account the Dirichlet and Neumann boundary conditions (2.15) and (2.16). Hence, the numerical diffusive flux at the boundaries is defined as

$$\mathcal{D}^n_{K,\sigma} := \begin{cases} \dfrac{m_\sigma \tilde{\kappa}^n_K}{d_{K,\sigma}}(T^n_K - 1) & \text{if } \sigma \in \mathcal{E}^{\text{ext}},\ x = x_{\text{a}}, \\ \dfrac{m_\sigma \tilde{\kappa}^n_K}{d_{K,\sigma}} T^n_K & \text{if } \sigma \in \mathcal{E}^{\text{ext}},\ x = x_{\text{b}}, \\ 0 & \text{if } \sigma \in \mathcal{E}^{\text{ext}},\ y = y_{\text{a}} \text{ or } y = y_{\text{b}}. \end{cases}$$

Then, for every $K = K_{i,j} \in \mathcal{T}$ and assuming that $\tilde{T}^{n+1/2}_{i,j}$ has been computed via (3.15), we handle the diffusive part of (2.9d) by the implicit scheme

$$T^{n+1}_{i,j} = \tilde{T}^{n+1/2}_{i,j} + \Delta t \sum_{\sigma \in \mathcal{E}_K} \mathcal{D}^{n+1}_{K,\sigma}. \tag{3.16}$$

Since $\mathcal{D}^{n+1}_{K,\sigma}$ depends linearly on T^{n+1}_K, (3.16) leads to a linearly implicit system in terms of the vector $\boldsymbol{T}^{n+1} = (T^{n+1}_K)_{K \in \mathcal{T}}$.

3.5 CFL condition

The explicit scheme (3.3), (3.4) that approximates (2.9a) needs to be supplemented with a suitable CFL condition to ensure its stability. Following [8], we assume that

$$\Delta t \le \Delta t^{n+1}_{\text{mass}} := \frac{\Delta y}{2(\max\{|\omega^{x,n}_{\max}|, |\omega^{y,n}_{\max}|\} + 1)}. \tag{3.17}$$

Here $\omega^{x,n}_{\max}$ and $\omega^{y,n}_{\max}$ are the maximal speeds of wave propagation in the x- and y-directions, respectively. For a piecewise constant approximation of $\boldsymbol{q}$ at $t = t^n$,

$$\omega^{k,n}_{\max} = \max\left\{ \left| \frac{\mathrm{d}F^k}{\mathrm{d}\phi}(q^n_K, \phi^n_K) \right| : \quad K \in \mathcal{T} \right\}, \quad k \in \{x, y\},$$

where the fluxes F^x and F^y are defined in (3.2). Note that since Δt^n_{mass} varies in each time iteration, our numerical scheme is adaptive. For the second heat equation, thanks to the semi-implicit approach given by equations (3.14), (3.15) and (3.16), the only restrictive part in terms of the time step is due to the convective term. Hence, given a piecewise constant approximation of $\boldsymbol{q}$ at $t = t^n$, the CFL condition arising from the heat equation is

$$\Delta t \le \Delta t^{n+1}_{\text{heat}} := \frac{1}{2} \min\left\{ \frac{\Delta x}{\|q^{x,n}\|_\infty}, \frac{\Delta y}{\|q^{y,n}\|_\infty} \right\}, \tag{3.18}$$

where $\|\cdot\|_\infty$ corresponds to the infinity norm on Ω. The above bound Δt^n_{heat} is also time-dependent since it varies with each time iteration. Having both restrictions for the time step, at each time iteration $t = t^n$, we set Δt as the minimum among the two restrictions (3.17) and (3.18) , this is

$$\Delta t = \min\left\{ \Delta t^n_{\text{mass}}, \Delta t^n_{\text{heat}} \right\}, \qquad n \ge 1. \tag{3.19}$$

The fully coupled numerical scheme requires a sufficiently small initial time step Δt^0.

3.6 Coupling strategy

The system (2.9) is approximated by an adaptive method that combines the discretizations of the three discrete sub-problems described above under the varying time step Δt following the CFL condition (3.19). The approximation of the solids volume fraction ϕ is computed by (3.3) and (3.4), the discrete velocity $\boldsymbol{q}$ and pressure p are obtained by solving the linear system (3.13), and the approximate temperature T is computed from (3.14) and (3.15) and the linear system (3.16).

Algorithm 1 (Marching formula and coupling procedure)

Input: ρ_{f}, ρ_{s}, β_{f}, κ_{s}, κ_{f}, $c_{\mathrm{p,f}}$, $c_{\mathrm{p,s}}$, λ, η, Δx, Δy
$\phi^n \leftarrow \phi_0, \quad T^n \leftarrow T_0, \quad \Delta t \leftarrow \Delta t^0$
$n \leftarrow 0$
while $t < t_{\mathrm{end}}$ **do**
  compute $\boldsymbol{q}^n$ and p^n from system (3.13) given ϕ^n, T^n ▷ solve perturbed Stokes system
  for $i = 1, \ldots, N_x$ **do**
    for $j = 1, \ldots, N_y$ **do**
      $\phi_{i,j}^{n+1/2} \leftarrow \phi_{i,j}^n - \frac{\Delta t}{\Delta x}\left(F_{i+1/2,j}^{x,n} - F_{i-1/2,j}^{x,n}\right)$ ▷ approx. (2.9a); x axis
      $T_{i,j}^{n+1/2} \leftarrow T_{i,j}^n - \frac{\Delta t}{\Delta x}\left(U_{i+1/2,j}^{x,n} - U_{i-1/2,j}^{x,n}\right)$ ▷ approx. convective (2.9d); x axis
    end for
  end for
  for $i = 1, \ldots, N_x$ **do**
    for $j = 1, \ldots, N_y$ **do**
      $\phi_{i,j}^{n+1} \leftarrow \phi_{i,j}^{n+1/2} - \frac{\Delta t}{\Delta y}\left(F_{i,j+1/2}^{y,n} - F_{i,j-1/2}^{y,n}\right)$ ▷ update ϕ from (2.9a)
      $\tilde{T}_{i,j}^{n+1/2} \leftarrow T_{i,j}^{n+1/2} - \frac{\Delta t}{\Delta y}\left(U_{i,j+1/2}^{y,n} - U_{i,j-1/2}^{y,n}\right)$ ▷ approx. convective (2.9d)
    end for
  end for
  compute $\boldsymbol{T}^{n+1}$ from (3.16) given $(\tilde{T}_K^{n+1/2})_{K\in\mathcal{T}}$ and ϕ^{n+1} ▷ update T from (2.9d)
  $\Delta t_{\mathrm{mass}} \leftarrow \Delta y/(2\omega_{\max} + 2)$
  $\Delta t_{\mathrm{heat}} \leftarrow \frac{1}{2}\min\left\{\Delta x/\|q^{x,n}\|_\infty, \Delta y/\|q^{y,n}\|_\infty\right\}$
  $\Delta t \leftarrow \min\{\Delta t_{\mathrm{heat}}, \Delta t_{\mathrm{mass}}\}$ ▷ update time step
  $t \leftarrow t + \Delta t$
  $n \leftarrow n + 1$
end while
compute $\boldsymbol{q}^n$ and p^n from system (3.13) given ϕ^n, T^n
return $\{(\phi^1, \boldsymbol{q}^1, p^1, T^1), \ldots, (\phi^n, \boldsymbol{q}^n, p^n, T^n)\}$

The main idea for the coupling is the following. At each time iteration, we begin by solving system (3.13) for $\boldsymbol{q}$ and p, both corresponding to time t^n, then with the updated velocity $\boldsymbol{q}^n$ we approximate ϕ using formulas (3.3) and (3.4), in this case corresponding to t^{n+1}. Then we use $\boldsymbol{q}^n$ and the updated volume fraction ϕ^{n+1} to update the temperature T. This procedure for the fully coupled numerical scheme including the marching formulas in time and space is described in Algorithm 1.

4 Numerical results

For all examples, we have implemented the numerical scheme described in Section 3 in the software Matlab. For the solution of the linear systems arising in (3.13) and (3.16), we make use of the backslash Matlab function. In addition, in all simulations, we use an initial time step $\Delta t^0 = 0.001$, constant room temperature $T_0 = 20\,^{\circ}\mathrm{C}$ and $x_{\mathrm{a}} = -1/2$, $x_{\mathrm{b}} = 1/2$, $y_{\mathrm{a}} = -2$ and $y_{\mathrm{b}} = 2$. For the batch flux and viscosity functions in (2.7) we set the exponents $n_{\mathrm{RZ}} = 2.0$ and $\alpha = 2.0$, respectively.

The rest of the parameters and constants are

$$\kappa_{\mathrm{s}} = 3\,\mathrm{W/mK}, \quad \kappa_{\mathrm{f}} = 5.8\times10^{-1}\,\mathrm{W/mK}, \quad c_{\mathrm{p,s}} = 7.41\times10^{2}\,\mathrm{J/kg}, \quad c_{\mathrm{p,f}} = 4.18\,\mathrm{J/kg},$$
$$\rho_{\mathrm{f}} = 1000\,\mathrm{kg/m^3}, \quad \rho_{\mathrm{s}} = 2650\,\mathrm{kg/m^3}, \quad \beta_{\mathrm{f}} = 2.07\times10^{-4}\,^{\circ}\mathrm{C}^{-1}, \tag{4.1}$$
$$\lambda = 9\times10^{3}, \quad \eta = 1\times10^{-5},$$

and v_0, g, ν_{f}, μ_{f}, Pr, L and Re are given in (2.10).

4.1 Simulation 1: Diehl test

We now assume that above a certain height y_{D}, the concentration is homogeneous and equal to ϕ_0, with pure water below. In our current setting, this initial condition reads as follows

$$\phi(x,y,0) = \begin{cases} \phi_0 & \text{if } y_{\mathrm{D}} \le y \le y_{\mathrm{b}}, \\ 0 & \text{if } 0 \le y < y_{\mathrm{D}}, \end{cases}$$

where $y_{\mathrm{D}} \in (y_{\mathrm{a}}, y_{\mathrm{b}})$. For this test, we keep $T(x,y,0) = 0$ in the entire domain and use an angle of inclination $\theta = 60°$. In addition, we set $y_{\mathrm{D}} = 1$, $\Delta x = \Delta y = 0.025$ and a total of 6400 control volumes. Figure 5 shows the simulation of the Diehl test at three time points; $t_1 = 0.0148$, $t_2 = 0.0336$ and $t_3 = t_{\mathrm{end}} = 1.4200$. The volume fraction (first column) initially loaded at the top of the vessel begins to descend, generating a "tongue" of mixture which settle until all solid particles are deposited at the bottom. Besides the thin layer of solid particles at the wall $x = x_{\mathrm{b}}$ for $t = t_3$, a horizontal solid-liquid interface is created as expected. The temperature profiles show that heat spreads at a slower pace than sedimentation, and evolves mostly through regions of the domain with clear water. With respect to pressure we observe that while particles are moving towards the bottom a higher pressure begins to appear towards the bottom as the sediment becomes concentrated. For the volume average velocity we observe circular regions in which the speed is maximum. The corresponding flow vectors, plotted in Figure 6, indicate that these circular regions indeed correspond to the circulation effect.

4.2 Simulation 2: comparison of two heat conditions

In the next two numerical experiments we change the temperature variation ΔT and the coefficient of thermal expansion β_{f}. For these examples, we use the same initial volume fraction $\phi = \phi_0 = 0.5$ and initial temperature $T = 0$ in Ω and $t = t_{\mathrm{end}} = 1$. The first example is produced with $\Delta T = 0\,^{\circ}\mathrm{C}$ (equivalently $T_{\mathrm{h}} = T_0$) and β_{f} given in (4.1). The second is made with a higher temperature variation $\Delta T = 40\,^{\circ}\mathrm{C}$ and an amplified coefficient of thermal expansion $\beta = 2.07\times10^{-2}\,^{\circ}\mathrm{C}^{-1}$. The result (see Figure 7) shows that apart from obvious changes in the temperature profiles, variations in the volume fraction are hardly observable. However, the velocity field exhibits variations near the top of the vessel clearly attributable to the change in temperature.

4.3 Simulation 3: analysis of clear liquid production and sediment

To measure the increase of efficiency in water recovery, we analyze the production of clear water under various angles and temperature combinations and measure for each numerical simulation the time quotient $\eta_{\mathrm{water}} := t^{\mathrm{ref}}_{\mathrm{water}}/t_{\mathrm{water}}$, where t_{water} is defined as the time point at which the total volume of water (clear liquid) reaches 90% of the total volume of the tank. Specifically, we convert the numerical values of the solids volume fraction ϕ into values of the water volume fraction $\phi_{\mathrm{water}} := 1 - \phi$, and a computational cell K is counted as part of the water forming as soon as $\phi_{\mathrm{water},K} > 0.98$, i.e., concept of clear water employed here refers to the regions within the domain in which the concentration of solids is less than 2%. The reference time $t^{\mathrm{ref}}_{\mathrm{water}}$ is defined in the same way for an angle $\theta = 90°$ (no inclination) and zero temperature variation $\Delta T = 0°\mathrm{C}$ (or $T_{\mathrm{c}} = T_0$).

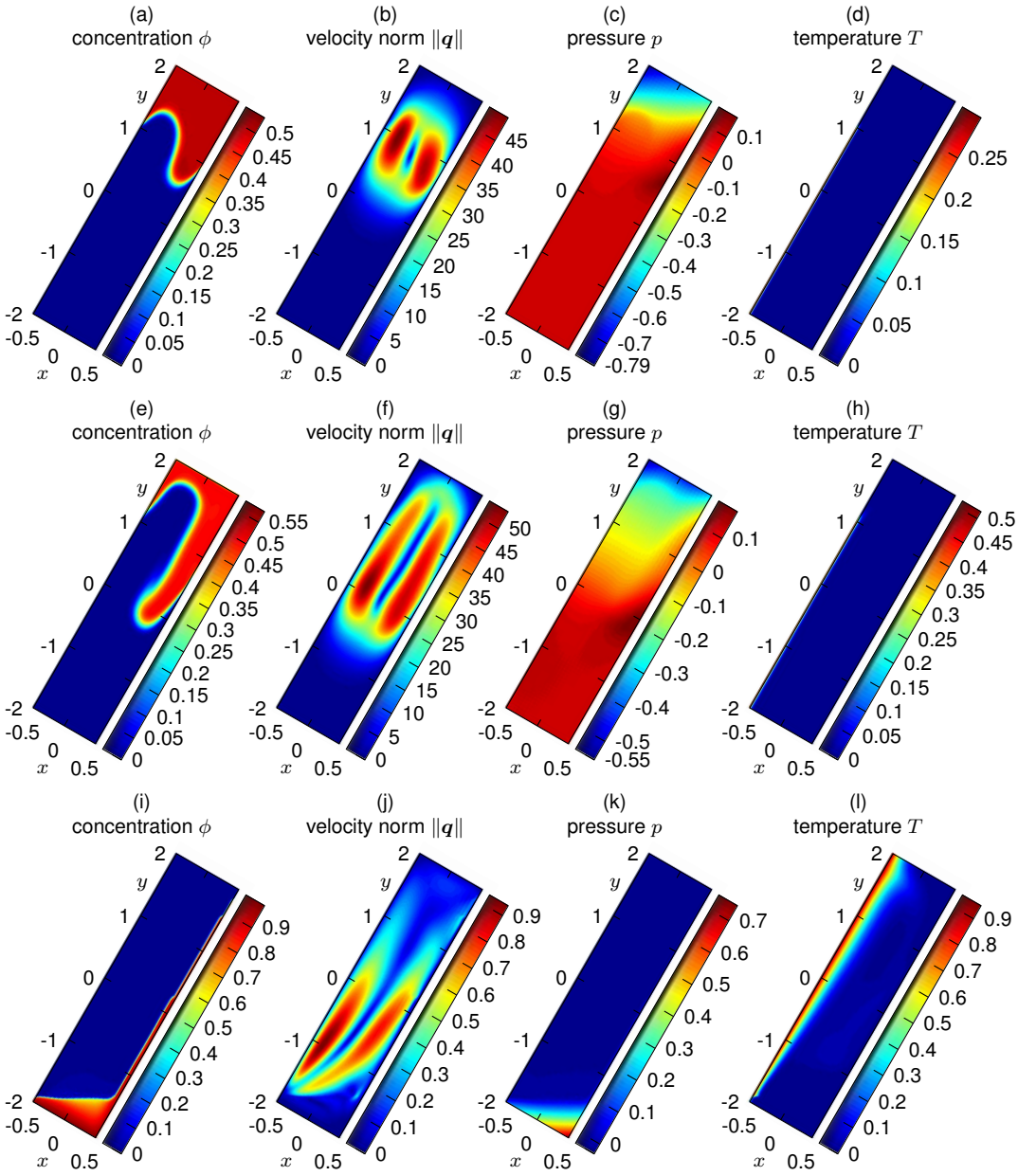

FIGURE 5. Simulation 1 (Diehl test) with $\theta = 60°$, $\Delta T = 20\,°\text{C}$ and $\phi_0 = 0.5$ for $y_\text{D} = 1$ at (first row) $t_1 = 0.0148$, (second row) $t_2 = 0.0336$ and (third row) $t_3 = t_\text{end} = 1.4200$.

To compute η_water we perform numerical simulations under various temperatures and angles of inclination, with $\Delta x = \Delta y = 0.05$ until t_water is reached. In Table 1, we report the efficiency coefficient for the numerical experiments varying $\theta = 90°, 80°, \ldots, 40°$ and temperature differences of $\Delta T = 0, 10, \ldots, 40\,°\text{C}$ with initial concentrations $\phi_0 = 0.1$, $\phi_0 = 0.2$, and $\phi_0 = 0.4$. (Selected cases for $\Delta T = 10\,°\text{C}$ are also illustrated in Figures 8 to 13, see below.) Results indicate, first of all,

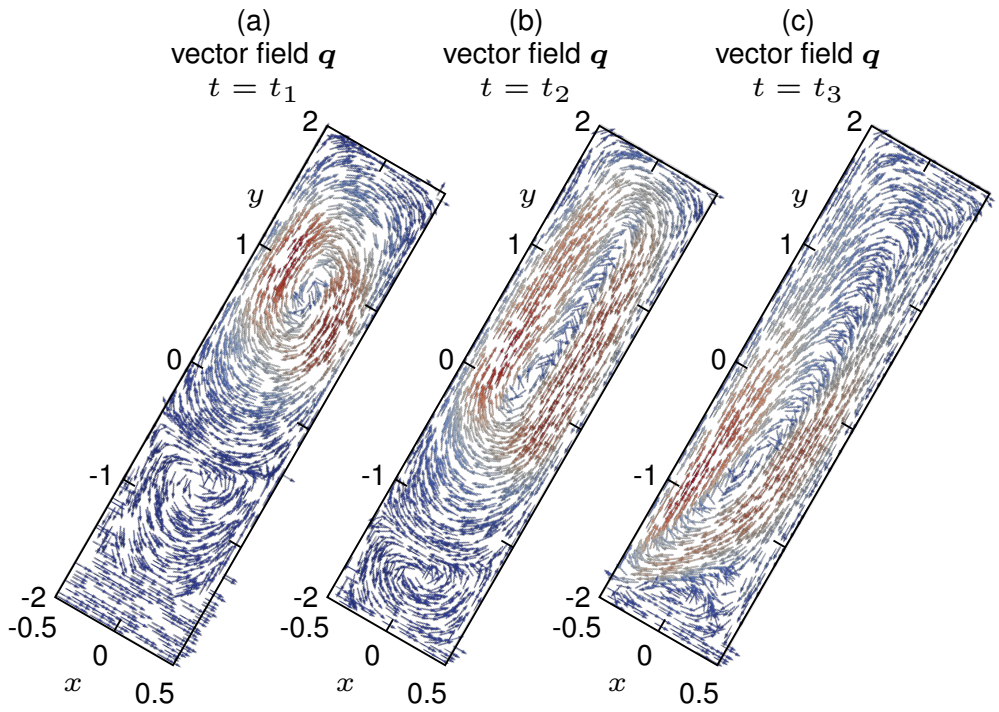

FIGURE 6. Simulation 1 (Diehl test) with $\theta = 60°$, $\Delta T = 20\,°\text{C}$ and $\phi_0 = 0.5$ for $y_\text{D} = 1$: velocity vector $\boldsymbol{q}$ at (a) $t_1 = 0.0148$, (b) $t_2 = 0.0336$ and (c) $t_3 = t_\text{end} = 1.4200$.

that inclination of the vessel always produces a gain in efficiency of at least 10% (for the values of θ tested). The degree of gain depends significantly on ϕ_0 and θ, but only marginally on ΔT. Notice that that for $\phi_0 = 0.1$ and $\phi_0 = 0.2$, the highest increase in efficiency is achieved for $\theta = 40°$. Only for $\phi_0 = 0.1$ we observe values of η_water larger than two. Furthermore, for the (hypothetical) case of a fairly concentrated initial suspension ($\phi_0 = 0.4$) we obtain the highest values of η_water, that is $\eta_\text{water} \approx 1.3$, for $\theta = 60°$. It is interesting to note that in this case there exists an optimal angle of inclination.

In a second analysis we measure the potential gain in efficiency (through inclination and heating) in terms of formation of the sediment. In this case, we define the efficiency indicator $\eta_\text{solid} := t^\text{ref}_\text{solid}/t_\text{solid}$, where t_solid is defined as the time point in which the amount of mass of solids at a concentration $\phi > 0.8$ reaches 90% of the total. Similarly to the previous time reference, $t^\text{ref}_\text{solid}$ is defined as t_solid for the case of no inclination $\theta = 90°$ and zero temperature variation $\Delta T = 0\,°\text{C}$. Note that here we define as "settled solid" those parts of the domain in which the solid concentration is greater than 80%. We utilize the same numerical simulations as for the computation of η_water. In Table 2 the observed values of η_solid for the corresponding numerical experiments are listed. Results are similar to those for η_water in that for given values of ϕ_0 and θ does not vary appreciably with ΔT in most cases. However, in many instances the gains in efficiency measured by η_solid related to ϕ_0 and θ differ visibly from those measured by η_water. For instance, the case $\phi_0 = 0.1$ and $\theta = 90°$ leads for $\Delta T > 0\,°\text{C}$ to values $\eta_\text{solid} \approx 0.8$, so there is even a loss of efficiency, while the same pair of parameters led to the best values of η_water. A closer inspection of the entries of Table 2 reveals that for $\phi_0 = 0.1$ there is no distinguished optimal angle of inclination (in terms of maximizing η_solid)

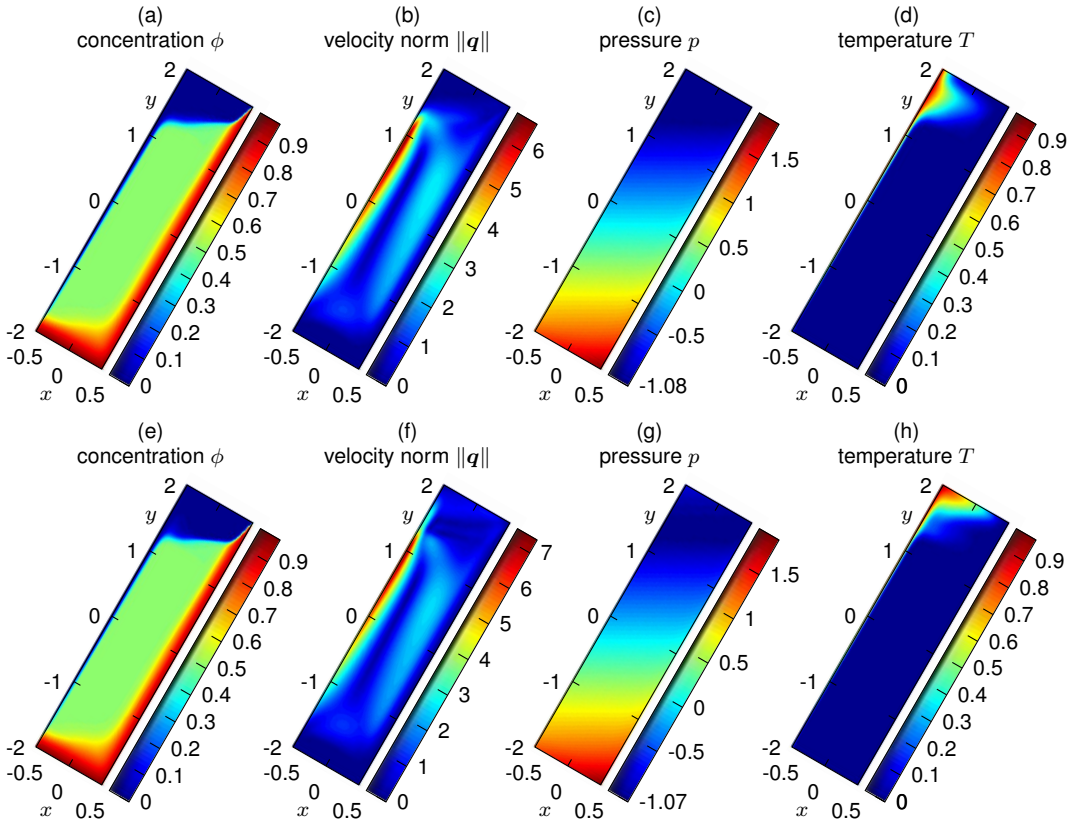

FIGURE 7. Simulation 2 (comparison of two heat conditions): batch sedimentation with $\theta = 60°$ and $\phi_0 = 0.5$ at $t = 1$ with (first row) $\Delta T = 5°\text{C}$ and $\beta_f = 2.07 \times 10^{-4}$ and (second row) $\Delta T = 40°\text{C}$ and $\beta_f = 2.07 \times 10^{-2}$.

while for $\phi_0 = 0.2$ and $\phi_0 = 0.4$ the optimal angle is $\theta = 40°$ (among the values tested). Notice, furthermore, that for $\phi_0 = 0.4$ and $\theta = 40°$, we have $\eta_{\text{water}} \approx 1.2$ but $\eta_{\text{solid}} \approx 1.8$.

Simulations under the scenarios described before for a fixed variation of temperature $\Delta T = 10\,°\text{C}$ varying the angle of inclination are presented in Figures 8 to 13. Figures 8, 10 and 12 show the simulations of the volume fraction at $t = 3$ computed with $\phi_0 = 0.1$, $\phi_0 = 0.2$ and $\phi_0 = 0.4$, respectively. Figures 9, 11 and 13 show the simulations of the temperature at $t = 3$ computed with $\phi_0 = 0.1$, $\phi_0 = 0.2$ and $\phi_0 = 0.4$, respectively. We observe that for angles close to 90°, at that time still a considerable portion of the mixture is present at the original concentration ϕ_0 while for $\theta = 50°$ or $\theta = 40°$, the separation is almost complete. These results of Figures 8, 10 and 12 are consistent with those obtained in [8] (where the iso-thermal case was treated and a smaller number of combinations of initial concentrations and inclination angles was discussed) and with analyses that involve experimental data (and are limited to the iso-thermal case as well), see [1, 22, 27, 32, 35, 44]. That said, it is noteworthy that Figures 9, 11 and 13 indicate that a considerable portion of the mixture becomes heated to the maximal temperature, and that the temperature distribution follows the upward stream of liquid, but that according to Tables 1 and 2, there is hardly any increase in efficiency due to convection. This result may well be explained by an inadequate adjustment of parameters in the present study such as the temperature difference applied, location and duration

TABLE 1. Simulation 3: efficiency coefficient η_{water} for various combinations of initial concentration ϕ_0, angle of inclination θ, and applied temperature difference ΔT. (Here and in Table 2, the entry "1" for $\Delta T = 0\,^{\circ}\text{C}$ and $\theta = 90^{\circ}$ indicates the reference value.)

ϕ_0	$\Delta T\,[^{\circ}\text{C}]$	$\theta = 90^{\circ}$	$\theta = 80^{\circ}$	$\theta = 70^{\circ}$	$\theta = 60^{\circ}$	$\theta = 50^{\circ}$	$\theta = 40^{\circ}$
	0	1	1.215070	1.447193	1.629246	1.864724	2.127147
	10	0.998308	1.218234	1.449904	1.631780	1.867789	2.124425
0.1	20	0.996914	1.215088	1.452628	1.629677	1.864581	2.121582
	30	0.997948	1.214746	1.450139	1.627519	1.867663	2.110494
	40	0.996198	1.215925	1.447670	1.625294	1.864499	2.107478
	0	1	1.249885	1.381455	1.530540	1.699557	1.966316
	10	1.001554	1.250289	1.381584	1.531768	1.694235	1.951882
0.2	20	1.000144	1.250637	1.381763	1.529472	1.684920	1.943776
	30	1.000500	1.250817	1.381987	1.530769	1.687113	1.929612
	40	1.000315	1.250694	1.382238	1.528604	1.696916	1.921460
	0	1	1.103264	1.179044	1.297321	1.264294	1.206245
	10	0.999611	1.106751	1.181789	1.301679	1.264293	1.202108
0.4	20	1.001250	1.105600	1.186230	1.304353	1.270945	1.204229
	30	1.001242	1.105028	1.186373	1.307331	1.277490	1.210443
	40	1.000194	1.104611	1.185703	1.307119	1.281623	1.218690

TABLE 2. Simulation 3: efficiency coefficient η_{solid} for various combinations of initial concentration ϕ_0, angle of inclination θ, and applied temperature difference ΔT.

ϕ_0	$\Delta T\,[^{\circ}\text{C}]$	$\theta = 90^{\circ}$	$\theta = 80^{\circ}$	$\theta = 70^{\circ}$	$\theta = 60^{\circ}$	$\theta = 50^{\circ}$	$\theta = 40^{\circ}$
	0	1	1.221111	1.303926	1.259727	1.310197	0.877267
	10	0.999255	1.220158	1.305909	1.259315	1.294494	0.792031
0.1	20	0.998618	1.221504	1.307935	1.258765	1.288716	0.800016
	30	0.997702	1.221718	1.304169	1.258108	1.286185	0.808227
	40	0.998959	1.219700	1.307614	1.257316	1.280646	0.813885
	0	1	1.179874	1.267256	1.370405	1.427996	1.566994
	10	0.997718	1.180092	1.264177	1.369244	1.433853	1.567584
0.2	20	0.997507	1.181715	1.264612	1.370823	1.439480	1.521487
	30	0.998763	1.182454	1.265060	1.369597	1.432235	1.518220
	40	0.999303	1.182337	1.265513	1.371144	1.434327	1.518475
	0	1	1.073771	1.215368	1.374468	1.559977	1.801505
	10	1.000917	1.073161	1.215618	1.375958	1.562195	1.803902
0.4	20	1.000068	1.074787	1.214544	1.373723	1.561252	1.802245
	30	1.000947	1.074353	1.214594	1.375496	1.560161	1.800374
	40	1.000615	1.073730	1.213830	1.374109	1.558926	1.802090

of heating and choice of parameters accounting for heat conduction and transport. However, it could also be that enhancement of circulation in itself does not necessarily accelerate clear liquid

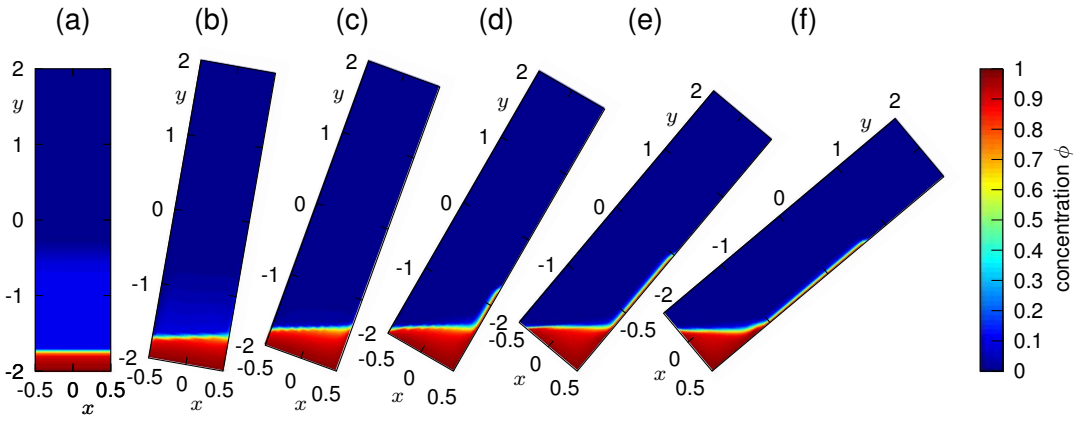

FIGURE 8. Simulation 3: simulated concentration ϕ at $t = 3$ for $\phi_0 = 0.1$. Here and in Figures 9 to 13, $\Delta T = 10$ °C, and the angles of inclination are (a) $\theta = 90°$, (b) $\theta = 80°$, (c) $\theta = 70°$, (d) $\theta = 60°$, (e) $\theta = 50°$ and (f) $\theta = 40°$.

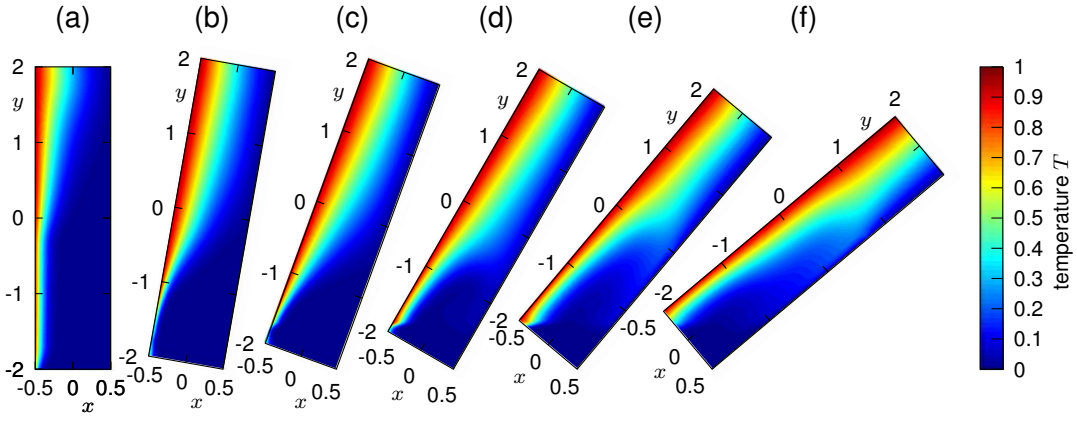

FIGURE 9. Simulation 3: simulated temperature T at $t = 3$ for $\phi_0 = 0.1$.

production and settling; for instance the upward-streaming portion of the circulation possibly accounts for (undesired) entrainment of particles.

4.4 Simulation 4: measuring improvements of settling time

A preliminary analysis of the numerical results of Simulations 1 to 3 indicates that although numerical results agree with experimental evidence and the numerical method works correctly, the conjectured improvement of separation efficiency, that is the acceleration of liquid production or sediment formation (as indicated in Tables 1 and 2) through additional heating is at most marginal. This property likely arises since the onset of convection is much slower, and the convection velocity is much smaller, than the velocity associated with the settling of particles. This conjecture is underlined by a simulation made for the convection of pure water ($\phi_0 = 0$) with $\Delta T = 40$°C and the two different choices of β_f utilized in Simulation 2 (see Figure 7). The simulated time, $t = 9$, is large enough so that both velocity fields can be considered stationary. The value $\beta_f = 2.07 \times 10^{-4}$, used in Figure 14 (a), is realistic for water and is the value used in Simulations 1 and 3. Notice that the norm of the velocity is at most 0.25, where velocity is refereed to v_0 (see (2.10)). This supports

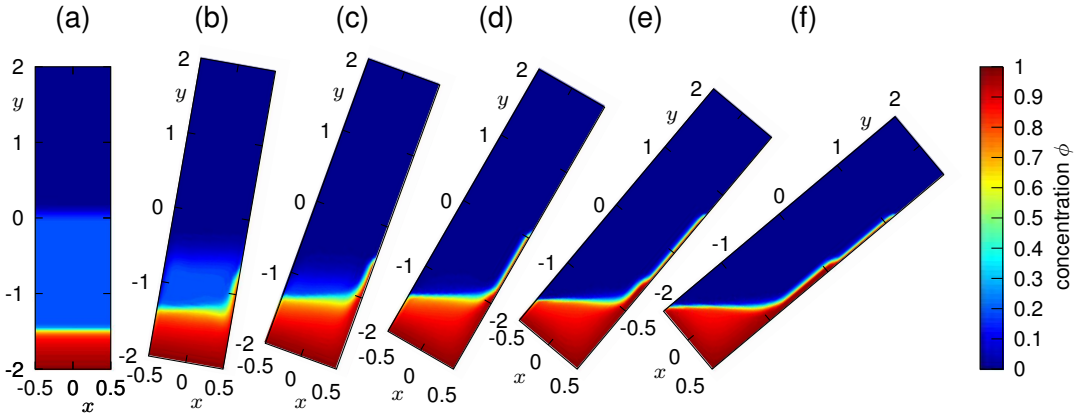

FIGURE 10. Simulation 3: simulated concentration ϕ at $t = 3$ for $\phi_0 = 0.2$.

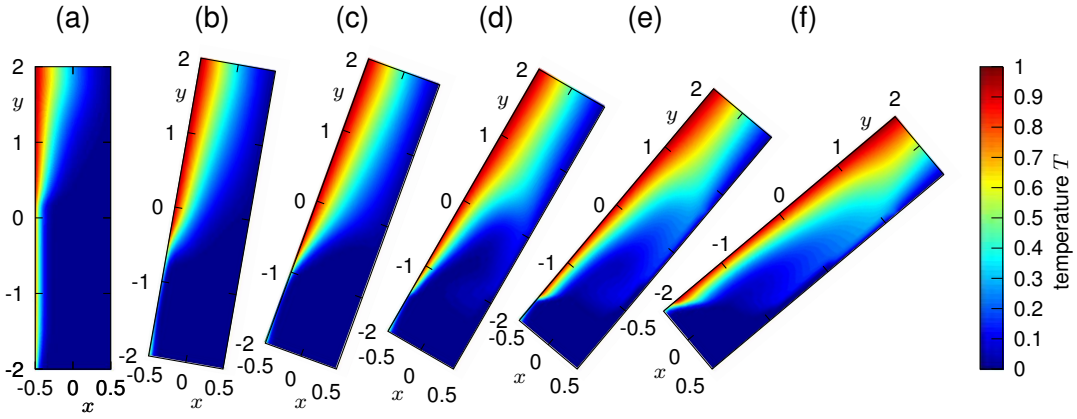

FIGURE 11. Simulation 3: simulated temperature T at $t = 3$ for $\phi_0 = 0.2$.

that the conjecture that in Simulations 1 and 3 the settling process, enhanced by the circulation due to inclination of the vessel, occurs significantly more rapidly than the onset of heat-driven convection, and that therefore the added effect of convection is marginal.

Finally, we show in Figure 14 (b) the same simulation for pure liquid but assuming that $\beta_f = 2.07 \times 10^{-2}$. This parameter is of course unrealistic, but we now observe a velocity field with velocities that are about 18 times larger than those of Figure 14 (a) for $\beta_f = 2.07 \times 10^{-4}$. This leads to the conjecture that increasing β_f may lead to more rapid convection that could lead to better visible separation efficiency in a simulation with $\phi_0 > 0$. In the dilute regime ($\phi \ll 1$) the dominating term in (2.8) is the second one, and it involves the factor $\lambda\beta_f$. Since for aqueous suspensions, β_f needs to be considered as a constant, one may attempt to produce evidence of heat-driven acceleration of the separation by increasing λ. Without compromising other parameters thus can be done by decreasing v_0, for example by assuming that the particle size is relatively small. Alternatively, one may assume that the density difference is relatively small, and increase the heat diffusivity. This has been done in Simulation 4 (see Figure 15), where we utilize $\rho_s = 1050\,\mathrm{kg/m^3}$ and $\rho_f = 1000\,\mathrm{kg/m^3}$ along with a function $\tilde{\kappa}$ increase by a factor 20, combined with a number of applied temperature differences. The quantity plotted in Figure 15 is the percentage of solids

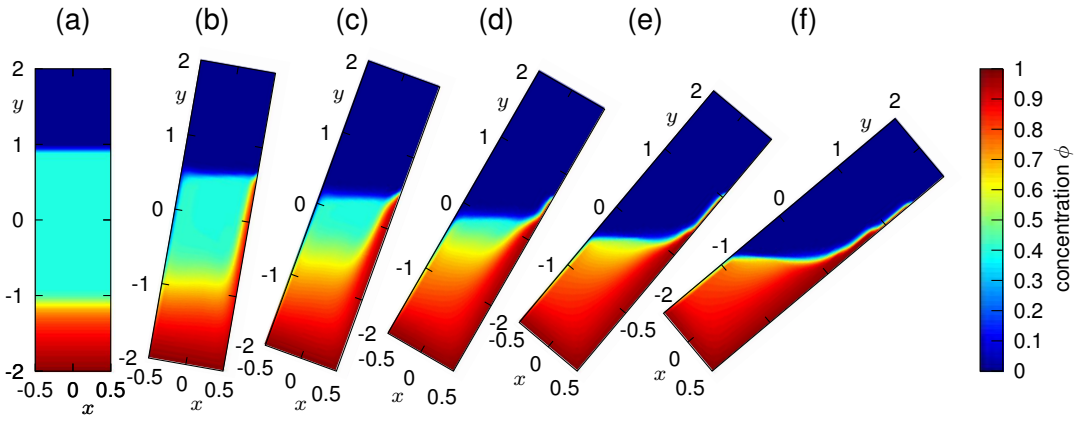

FIGURE 12. Simulation 3: simulated concentration ϕ at $t = 3$ for $\phi_0 = 0.4$.

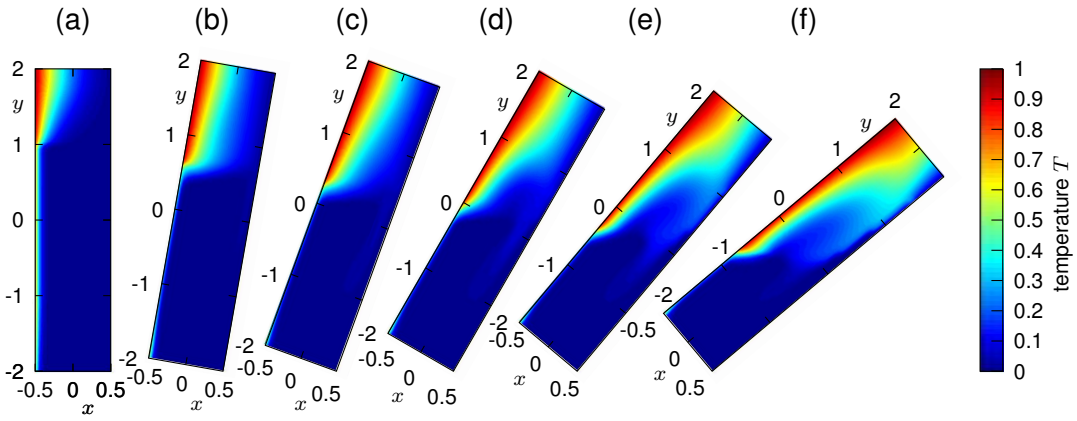

FIGURE 13. Simulation 3: simulated temperature T at $t = 3$ for $\phi_0 = 0.4$.

trapped in sediment, that is in a region with solids concentration over 0.9. The enlarged views (Figure 15 (b), (d) and (f)) indicate that this percentage consistently grows more rapidly with increasing applied temperature ΔT.

5 Conclusions

We have proposed a two-dimensional mathematical model to simulate the sedimentation process in inclined vessels (known as the Boycott experiment) under the presence of heat sources. The resulting governing equations signify an extension to the model presented in [8, 9, 11], where the novelty resides in the addition of the temperature distribution described through the heat equation. Using the Boussinesq approximation, we end up coupling the heat equation by means of a temperature-dependent source term in the momentum balance. The two phenomena, gravity settling, and induced natural convection, interact as driving forces for the studied process. The adaptive finite volume numerical scheme proposed to approximate the equations is built taking into account the nonlinear flux present in the concentration equation, the solution of the linearly implicit system

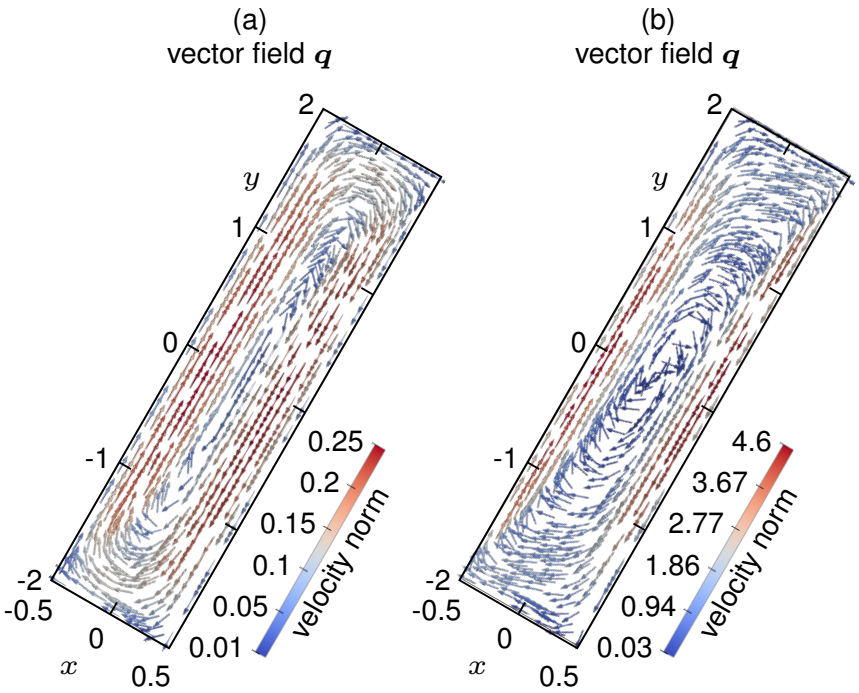

FIGURE 14. Velocity field for convection of pure fluid ($\phi_0 = 0$) for $\theta = 60°$ at $t = 9$ with $\Delta T = 40°$C (a) $\beta_f = 2.07 \times 10^{-4}$, (b) $\beta_f = 2.07 \times 10^{-2}$.

arising from the perturbed Stokes system with nonlinear viscosity function, and a semi-implicit time approximation for the heat equation. The adaptive treatment of the time step, added to the implicit resolution of the nonlinear diffusive term at the heat equation, allows the use of time steps that are not so restrictive, thereby increasing the speed of the simulations. Through a series of numerical examples, we have shown that the application of heat can increase the settling velocity of suspended particles. This phenomenon can be explained by density changes of the liquid and to a lesser extent, due to the reduction in its viscosity, which causes a natural convection that modifies the velocity field of the mixture. In the main example, Simulation 3 (Section 4.3), the effect of the heat source is overshadowed by gravity settling, leading to a minimal effect on water recovery. However, in Simulation 4 (Section 4.4), it is shown that under changes in the parameters, the velocity field induced by the heat source can get the order of magnitude of the velocity generated by the solid-liquid density differences. On the other hand, we observe that the initial conditions modify the results, as it was pointed out in Simulation 3, where the temperature profile is reached much later in the numerical experiments, when most of the solid has been settled.

The findings reported in this article have significant applications in various industries, from wastewater treatment to mineral separation in mining. The ability to accelerate the settling of particles in a controlled manner can result in significant savings in time and energy, in addition to improving the efficiency of different processes developed in the industry. Heat-assisted sedimentation represents an interesting technique that deserves further research and development. Its potential to optimize processes and improve efficiency in a variety of applications makes it an area for future study and practical uses. Further studies can be done by considering different geometries in two and three dimensions, testing different batch flux functions, and the use of advanced

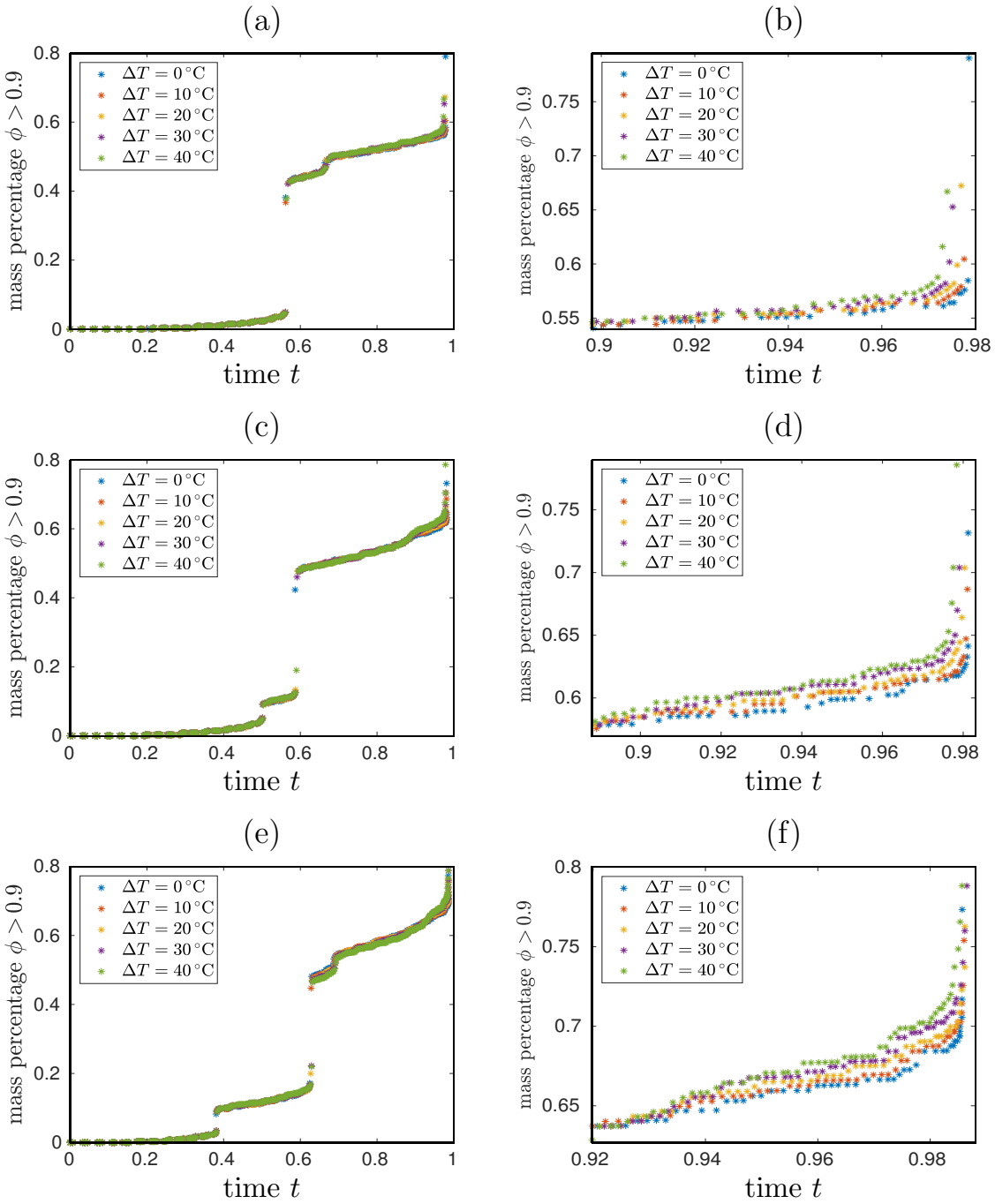

FIGURE 15. Simulation 4: evolution of the percentage of solids concentrated at more than 90% for (a) $\theta = 40°$, (b) enlarged view of (a), (c) $\theta = 50°$, (d) enlarged view of (c), (e) $\theta = 50°$ and (f) enlarged view of (e), starting from $\phi_0 = 0.05$.

numerical methods such as discontinuous Galerkin or mixed finite elements. In addition, another interesting focus to continue with this research is to compare our numerical scheme with experiments carried out under operational conditions in the industry. A future extension of this work

can be the addition of the neglected terms arising from the nonlinear Navier-Stokes equations in its transient version, and studying the impact of our quasi static approach in the simulations.

Acknowledgements

F.B. and R.B. are supported by ANID (Chile) projects Anillo ANID/ACT210030; Centro de Modelamiento Matemático (CMM), projects ACE210010 and FB210005 of BASAL funds for Centers of Excellence; and CRHIAM, projects ANID/FONDAP/15130015 and ANID/FONDAP/1523A0001. In addition R.B. is supported by ANID (Chile) through Fondecyt project 1210610. J.C. is supported by ANID through Fondecyt project 3230553.

References

[1] A. Acrivos, and E. Herbolzheimer. Enhanced sedimentation in settling tanks with inclined walls, *J. Fluid Mech.* 92:435–457, 1979.
[2] F. Auteri, N. Parolini, and L. Quartapelle. Numerical investigation on the stability of singular driven cavity flow, *J. Comput. Phys.* 183:1–25, 2002.
[3] R. B. Bird, W. E. Stewart, and E. N. Lightfoot. *Transport Phenomena*, second revised ed., Wiley, 2007.
[4] A. E. Boycott. Sedimentation of blood corpuscles, *Nature* 104:532, 1920.
[5] R. Bürger, J. Careaga, and S. Diehl. A review of flux identification methods for models of sedimentation. *Water Sci. Tech.* 81:1715–1722, 2020.
[6] R. Bürger, R. Donat, P. Mulet and C. A. Vega. On the hyperbolicity of certain models of polydisperse sedimentation, *Math. Meth. Appl. Sci.* 35:723-744, 2012.
[7] R. Bürger and M. Kunik. A critical look at the kinematic-wave theory for sedimentation-consolidation processes in closed vessels, *Math. Meth. Appl. Sci.* 24:1257–1273, 2001.
[8] R. Bürger, R. Ruiz-Baier, K. Schneider, and H. Torres. A multiresolution method for the simulation of sedimentation in inclined channels, *Int. J. Numer. Anal. Model.* 9:479–504, 2012.
[9] R. Bürger, R. Ruiz-Baier, and H. Torres. A stabilized finite volume element formulation for sedimentation-consolidation processes, *SIAM J. Sci. Comput.* 34:B265–B289, 2012.
[10] R. Bürger and W. L. Wendland. Entropy boundary and jump conditions in the theory of sedimentation with compression, *Math. Meth. Appl. Sci.* 21:865-882, 1998.
[11] R. Bürger, W. L. Wendland, and F. Concha. Model equations for gravitational sedimentation-consolidation processes, *ZAMM Z.Angew. Math. Mech.* 80:79–92, 2000.
[12] M. C. Bustos, F. Concha, R. Bürger, and E. M. Tory. *Sedimentation and Thickening: Phenomenological Foundation and Mathematical Theory*, Kluwer Academic Publishers, Dordrecht, The Netherlands, 1999.
[13] M. C. Bustos, F. Paiva, and W. L. Wendland. Control of continuous sedimentation of ideal suspensions as an initial and boundary value problem, *Math. Meth. Appl. Sci.*, 12:533—548, 1990.
[14] M. C. Bustos, F. Paiva, and W. L. Wendland. Entropy boundary conditions in the theory of sedimentation of ideal suspensions, *Math. Meth. Appl. Sci.*, 19, 679–697, 1996.
[15] J. Careaga and G. N. Gatica. Coupled mixed finite element and finite volume methods for a solid velocity-based model of multidimensional sedimentation, *ESAIM: Math. Model. Numer. Anal.*, 57(4):2529–2556, 2023.
[16] J. Careaga and S. Diehl. Entropy solutions and flux identification of a scalar conservation law modelling centrifugal sedimentation, *Math. Meth. Appl. Sci.* 43(7):4530–4557, 2020.
[17] M. A. Christon, P. M. Gresho, and S. B. Sutton. Computational predictability of time dependent natural convection flows in enclosures (including a benchmark solution), *Int. J. Numer. Methods Fluids* 40:953–980, 2002.
[18] S. Diehl. Estimation of the batch-settling flux function for an ideal suspension from only two experiments, *Chem. Eng. Sci.* 62:4589–4601, 2007.
[19] H.-S. Dou, G. Jiang, and C. Lei. Numerical simulation and stability study of natural convection in an inclined rectangular cavity, *Math. Probl. Engrg.* article 198695, 2013.

[20] R. Eymard, R. Herbin, and J. C. Latché. Convergence analysis of a collocated finite volume scheme for the incompressible Navier-Stokes equations on general 2D or 3D meshes, *SIAM J. Numer. Anal.* 45:1–36, 2007.
[21] S. K. Godunov. Finite difference methods for numerical computation of discontinuous solutions of equations of fluid dynamics, *Mat. Sb.* 47:271–295, 1959 (in Russian).
[22] W. Graham and R. Lama. Sedimentation in inclined vessels, *Canad. J. Chem. Engrg.* 41:31–32, 1963.
[23] D. Kleine and B. D. Reddy. Finite element analysis of flows in secondary settling tanks, *Int. J. Numer. Meth. Engrg.* 64:849–876, 2005.
[24] G. J. Kynch. A theory of sedimentation, *Trans. Faraday Soc.* 48:166–176, 1952.
[25] M. Latsa, D. Assimacopoulos, A. Stamou, and N. C. Markatos. Two-phase modeling of batch sedimentation, *Appl. Math. Model.* 23:881–897, 1999.
[26] S. J. McCaffery, L. Elliott, and D. B. Ingham. One-dimensional enhanced sedimentation in inclined fracture channels, *Math. Engrg. Indust.* 6:261–290, 1998.
[27] S. J. McCaffery, L. Elliott, and D. B. Ingham. Two-dimensional enhanced sedimentation in inclined fracture channels, *Math. Engrg. Indust.* 7:97–125, 1998.
[28] H. Nakamura and K. Kuroda. La cause de l'accéleration de la vitesse de sédimentation des suspensions dans les recipients inclinés, *Keijo J. Medicine* 8:256–296, 1937.
[29] D. R. Oliver and V. G. Jenson. The inclined settling of dispersed suspensions of spherical particles in square-section tubes, *Canad. J. Chem. Engrg.* 42:191–195, 1964.
[30] S. Ostrach. Natural convection in enclosures, *Adv. Heat Transf.* 8:161–227, 1972.
[31] S. V. Patankar. *Numerical Heat Transfer and Fluid Flow*, Hemisphere, Washington, 1980.
[32] K. W. Pearce. Settling in the presence of downward-facing surfaces. In: P. A. Rottenburg (Ed.), *Proc. Symp. on the Interaction Between Fluids and Particles: 3rd Congress of the European Federation of Chemical Engineering*, London, June 20–22, 1962, pp. 30–39. Institution of Chemical Engineers, London, 1962.
[33] E. Ponder. On sedimentation and rouleaux formation—I, *Quart. J. Exper. Physiol.* 15:235–252, 1925.
[34] C. Reyes, M. Alvarez, C. F. Ihle, M. Contreras, and W. Kracht. The influence of seawater on magnetite tailing rheology, *Minerals Eng.* 131:363–369, 2019.
[35] C. Reyes, C. F. Ihle, F. Apaz, and L. A. Cisternas. Heat-assisted batch settling of mineral suspensions in inclined containers, *Minerals* 9:article 228, 2019.
[36] J. F. Richardson and W. N. Zaki. Sedimentation and fluidisation: Part I. *Trans. Inst. Chem. Engts.* (London) 32:35–53, 1954.
[37] R. Ruiz-Baier and I. Lunati. Mixed finite element-discontinuous finite volume element discretization of a general class of multicontinuum models, *J. Comput. Phys.* 322:666–688, 2016.
[38] R. Ruiz-Baier and H. Torres. Numerical solution of a multidimensional sedimentation problem using finite volume-element methods, *Appl. Numer. Math.* 95:280–291, 2015.
[39] W. Schneider. Kinematic-wave theory of sedimentation beneath inclined walls, *J. Fluid Mech.* 120:323–346, 1982.
[40] O. Shishkina and S. Horn. Thermal convection in inclined cylindrical containers, *J. Fluid Mech.* 790:article R3, 2016.
[41] M. Ungarish. *Hydrodynamics of Suspensions*, Springer-Verlag, Berlin, 1993.
[42] A. T. Unwin. The mixed convection flow of Newtonian and non-Newtonian fluids in a vertical fracture, *Math. Engng. Ind.* 5:59–76, 1994.
[43] T. Wan, S. Aliabadi, and C. Bigler. A hybrid scheme based on finite element/volume methods for two immiscible fluid flows, *Int. J. Numer. Methods Fluids* 61:930–944, 2009.
[44] E. Zahavi and E. Rubin. Settling of solid suspensions under and between inclined surfaces, *Ind. Engrg. Chem. Process Des. Dev.* 14:34–41, 1975.

Centro de Investigación en Ingeniería Matemática (CI^{2}MA)

PRE-PUBLICACIONES 2023 - 2024

2023-29 Rodolfo Araya, Fabrice Jaillet, Diego Paredes, Frederic Valentin: *Generalizing the Multiscale Hybrid-Mixed Method for Reactive-Advective-Diffusive Equations*

2023-30 Jessika Camaño, Ricardo Oyarzúa, Miguel Serón, Manuel Solano: *A mass conservative finite element method for a nonisothermal Navier-Stokes/Darcy coupled system*

2023-31 Franz Chouly, Hao Huang, Nicolás Pignet: *HHT-α and TR-BDF2 schemes for Nitsche-based discrete dynamic contact*

2024-01 Sergio Caucao, Gabriel N. Gatica, Saulo Medrado, Yuri D. Sobral: *Nonlinear twofold saddle point-based mixed finite element methods for a regularized $\mu(I)$-rheology model of granular materials*

2024-02 Julio Careaga, Gabriel N. Gatica, Cristian Inzunza, Ricardo Ruiz-Baier: *New Banach spaces-based mixed finite element methods for the coupled poroelasticity and heat equations*

2024-03 Harold D. Contreras, Paola Goatin, Luis M. Villada: *A two-lane bidirectional nonlocal traffic model*

2024-04 Rommel Bustinza, Matteo Cicuttin, Ariel Lombardi: *A Hybrid High-Order method for the mixed Steklov eigenvalue problem*

2024-05 Isaac Bermudez, Jaime Manríquez, Manuel Solano: *A hybridizable discontinuous Galerkin method for Stokes/Darcy coupling in dissimilar meshes*

2024-06 Thomas Führer, Diego Paredes: *Robust hybrid finite element methods for reaction-dominated diffusion problems*

2024-07 Raimund Bürger, Enrique D. Fernández Nieto, Jorge Moya: *A multilayer shallow water model for tsunamis and coastal forest interaction*

2024-08 Fernando Betancourt, Raimund Bürger, Stefan Diehl, María Carmen Martí, Yolanda Vásquez: *A degenerating convection-diffusion model of a flotation column: theory, numerics and applications*

2024-09 Fernando Betancourt, Raimund Bürger, Julio Careaga, Lucas Romero: *Coupled finite volume methods for settling in inclined vessels with natural convection*

Para obtener copias de las Pre-Publicaciones, escribir o llamar a: Director, Centro de Investigación en Ingeniería Matemática, Universidad de Concepción, Casilla 160-C, Concepción, Chile, Tel.: 41-2661324, o bien, visitar la página web del centro: http://www.ci2ma.udec.cl







Centro de Investigación en
Ingeniería Matemática (CI²MA)
Universidad de Concepción

Casilla 160-C, Concepción, Chile
Tel.: 56-41-2661324/2661554/2661316
http://www.ci2ma.udec.cl